# Crustal deformation across the Sierra Nevada, northern Walker Lane, Basin and Range transition, western United States measured with GPS, 2000–2004

William C. Hammond[1] and Wayne Thatcher[2]

Received 12 July 2006; revised 27 November 2006; accepted 15 December 2006; published 12 May 2007.

[1] Global Positioning System (GPS) data collected in campaigns in 2000 and 2004 were processed and interpreted with other GPS data in the western Basin and Range province to provide new constraints on the rate, style, and pattern of deformation of the central and northern Walker Lane (WL), which lies near the western boundary of the Basin and Range. Across the central WL, near 38°N latitude, the velocities with respect to North America increase westward by ~10 mm/yr inducing dextral shear. Farther north between 40° and 41°N latitude, a western zone of ~7 mm/yr relative motion undergoes dextral shear, and an eastern zone of ≤3 mm/yr relative motion undergoes extension and shear. These data show that the northern WL is essentially a dextral shear zone experiencing minor net dilatation ($\varepsilon_\Delta$ = 2.6 ± 0.8 nstrain/yr). Near most Holocene normal faults, dilatation inferred from the velocity field is not greater than the uncertainties. However, near the central Nevada seismic belt we detect significant dilatation expressed as extension in a direction approximately normal to the range fronts ($\varepsilon_\Delta$ = 23.0 ± 3.9 nstrain/yr), some of which is attributable to transient postseismic deformation following large historic earthquakes. A block model constrained by velocities corrected for transient effects shows that the sum of dextral slip rates across the Honey Lake, Warm Springs, east Pyramid fault system, and Mohawk Valley faults is ~7 mm/yr. The WL is a zone whose width and dilatation rate increase northwestward, consistent with counterclockwise rotation of the Sierra Nevada microplate and transfer of deformation into the Pacific Northwest.

**Citation:** Hammond, W. C., and W. Thatcher (2007), Crustal deformation across the Sierra Nevada, northern Walker Lane, Basin and Range transition, western United States measured with GPS, 2000–2004, *J. Geophys. Res.*, *112*, B05411, doi:10.1029/2006JB004625.

## 1. Introduction

[2] The Walker Lane (WL) is an intracontinental zone of strike-slip and normal faulting that is an important element of the Pacific–North America plate boundary region. It works closely with its companion, the San Andreas fault system to the west, to accommodate the ~50 mm/yr of relative motion between the Pacific and North American plates in the western United States. While the San Andreas system accommodates the majority of this displacement, roughly 25% of this motion occurs east of the Sierra Nevada in the Basin and Range province, where strike-slip and normal faulting are associated with active seismicity and deformation. Because of the pervasive normal faulting that has created the characteristic topography from which it gets its name, the Basin and Range is considered an extensional province [e.g., *Atwater and Stock*, 1998; *Wernicke and Snow*, 1998; *Sonder and Jones*, 1999]. However, geodetic studies have found that like the San Andreas, the majority of the deformation that occurs here is shear deformation [*Bennett et al.*, 2003; *Hammond and Thatcher*, 2004] whose net transport direction is parallel to the motion of the Sierra Nevada/Great Valley microplate (SNGV) with respect to North America. Direct geodetic observation of the area growth (dilatation), or widening of the province is more difficult because of its low rate compared to the shear deformation. Candidate processes behind the widening of the province include (1) gravitational collapse within the province [*Jones et al.*, 1996], or basal tractions beneath it that push the SNGV away from stable North America [e.g., *Atwater and Stock*, 1998], (2) extrusion of the Basin and Range toward Cascadia [*Humphreys and Hemphill-Haley*, 1996; *Wells and Simpson*, 2001], and (3) misalignment of the Sierra Nevada/Basin and Range boundary with respect to SNGV motion that introduces an extensional component to the relative motion causing area growth east of the SNGV [*Unruh et al.*, 2003; *Oldow*, 2003; *Kreemer et al.*, 2007]. While the net area growth rate of the province is positive, extension has not yet been well quantified or located well

[1]Nevada Bureau of Mines and Geology and Nevada Seismological Laboratory, University of Nevada, Reno, Nevada, USA.
[2]U.S. Geological Survey, Menlo Park, California, USA.


0148-0227/07/2006JB004625$09.00

enough to be used in distinguishing among the proposed mechanisms of Basin and Range extension.

[3] In this study we consider GPS measurements from a spatially distributed network of bench marks that constrain the deformation of the westernmost and most rapidly deforming part of the Basin and Range. We present results from three new campaign GPS networks that bound a transition in the pattern of the contemporary shear and extension that is focused inside the westernmost 100–300 km of the province. South of latitude 39°N, the zone of shear is focused inside a zone ~100 km wide [*Oldow et al.*, 2001]. North of latitude 39°N the zone widens and splits into a northwest trending zone of dextral shear, and a north-northeast trending zone of shear and extension [*Savage et al.*, 1995; *Svarc et al.*, 2002; *Kreemer et al.*, 2007]. Much of the deformation within the north-northeast trending zone can be attributed to postseismic relaxation from the historic earthquakes of the central Nevada seismic belt (CNSB) [*Hetland and Hager*, 2003; *Hammond and Thatcher*, 2004; *Gourmelen and Amelung*, 2005]. However, after subtracting the estimated effects of relaxation significant deformation remains, implying that the zone of secular deformation widens to the north [*Hammond et al.*, 2007].

[4] Here we demonstrate quantitatively that northward widening of the zone delineated by GPS in the WL is consistent with the previous suggestion that northwest directed shear in the WL is transferred into northwest-southeast extension across normal faults of the CNSB and vicinity. North of the CNSB the pattern of present-day deformation is not as well defined. *Hammond and Thatcher* [2005] used GPS survey results in the northwest Basin and Range of Nevada, California, and Oregon to suggest the existence of 3 small quasi-rigid blocks, with a north trending boundary of approximately east-west extension to the north of the CNSB in northern Nevada and southern Oregon and an east-west zone of approximately north-south compression in northernmost California. However, neither the distribution of GPS sites nor the accuracy of the measurements was sufficient to precisely locate these deforming zones or to define the other boundaries of these blocks. In this study we use additional data and block modeling to show that this east-west extension north of the CNSB is most likely localized on at least two normal to oblique fault systems between the CNSB and Surprise Valley in northeast California and likely not concentrated onto any single system in northwest Nevada.

## 2. Data

[5] The monuments surveyed in this study can be divided into three distinct subnetworks that span different segments of the western Great Basin. The northernmost network (Pyramid, Figure 1) spans the northern Walker Lane and extends northeast ~300 km from Lake Oroville, California, to Winnemucca, Nevada. The network to the south and east (Lovelock, Figure 1) spans ~200 km, crossing the CNSB near latitude 40°N, traversing several Basin and Range normal fault systems, including Dixie Valley, Shoshone Range, Carico Lake Valley, Western Toiyabe range, and Simpson Park Mountains fault zones. The southernmost network (Hawthorne, Figure 1) spans the central Walker Lane between latitude 38°N and 39°N, with the westernmost site lying at Tioga Pass inside Yosemite National Park on the SNGV block. The network extends ~200 km northeast to approximately Gabbs, Nevada, and lies approximately perpendicular to the average approximately N35°W trend of this transtensional fault system.

[6] Campaign surveys were conducted in 2000 and 2004, with at least two 6-hour sessions obtained for each site during each campaign. Some sites were occupied for a greater number of days, or for as many as three 24 hour sessions per campaign, because they were of particular interest, or were surveyed for other U.S. Geological Survey purposes, or because their remote locations permitted operating the GPS receiver unattended. A few sites were surveyed as many as 7 days in a single year, but the vast majority was surveyed 2–4 days. Bench marks for which only one daily session was obtained in 2000 or 2004 were not used in this study.

[7] Campaign bench marks consist of stable preexisting marks installed by various federal or state agencies (e.g., U.S. Geological Survey (USGS), U.S. Coast and Geodetic Survey, California Department of Transportation, U.S. Bureau of Reclamation). A few bench marks are USGS steel pins that are fixed to bedrock or concrete piers. Survey tripods were used to position the GPS antenna vertically over the geodetic bench mark. Height of the antenna phase center above the monument varied by as much as one meter from survey to survey, so measurements of the antenna height above the monument were made in triplicate during each occupation. Once a position was obtained for the antenna phase center, this correction plus a correction that accounts for the difference between the antenna phase center and the antenna reference point was applied to the vertical coordinate so that the position solution refers to the bench mark itself.

### 2.1. Data Processing

[8] All of the GPS data collected during these campaigns was processed using the GIPSY/OASIS II software package from the Jet Propulsion Laboratory (JPL). In addition to the data collected during these surveys, we also processed all of the data from prior USGS campaign surveys in the Basin and Range province and data from selected continuously recording GPS receivers of the BARGEN, BARD, and PANGA GPS networks collected after 1 January 1999. Continuous sites were included if they lay within or near the footprint of the Pyramid, Hawthorne, or Lovelock campaign networks (Table 1 and auxiliary material Table S1).[1] The same processing strategy, outlier identification, regional filtering, and reference frame adjustment were homogenously applied for all the data. Station coordinates were estimated every 24 hours using the precise point positioning method [*Zumberge et al.*, 1997] with ambiguity resolution applied across the entire network by automatic selection of either the ionospheric or pseudorange wide lane method [*Blewitt*, 1989]. Satellite orbit and clock parameters, and parameters permitting daily coordinate transformation into the global reference frame (ITRF2000) were provided by JPL. Ionosphere-free combinations of

[1] Auxiliary materials are available at ftp://ftp.agu.org/apend/jb/2006jb004625.

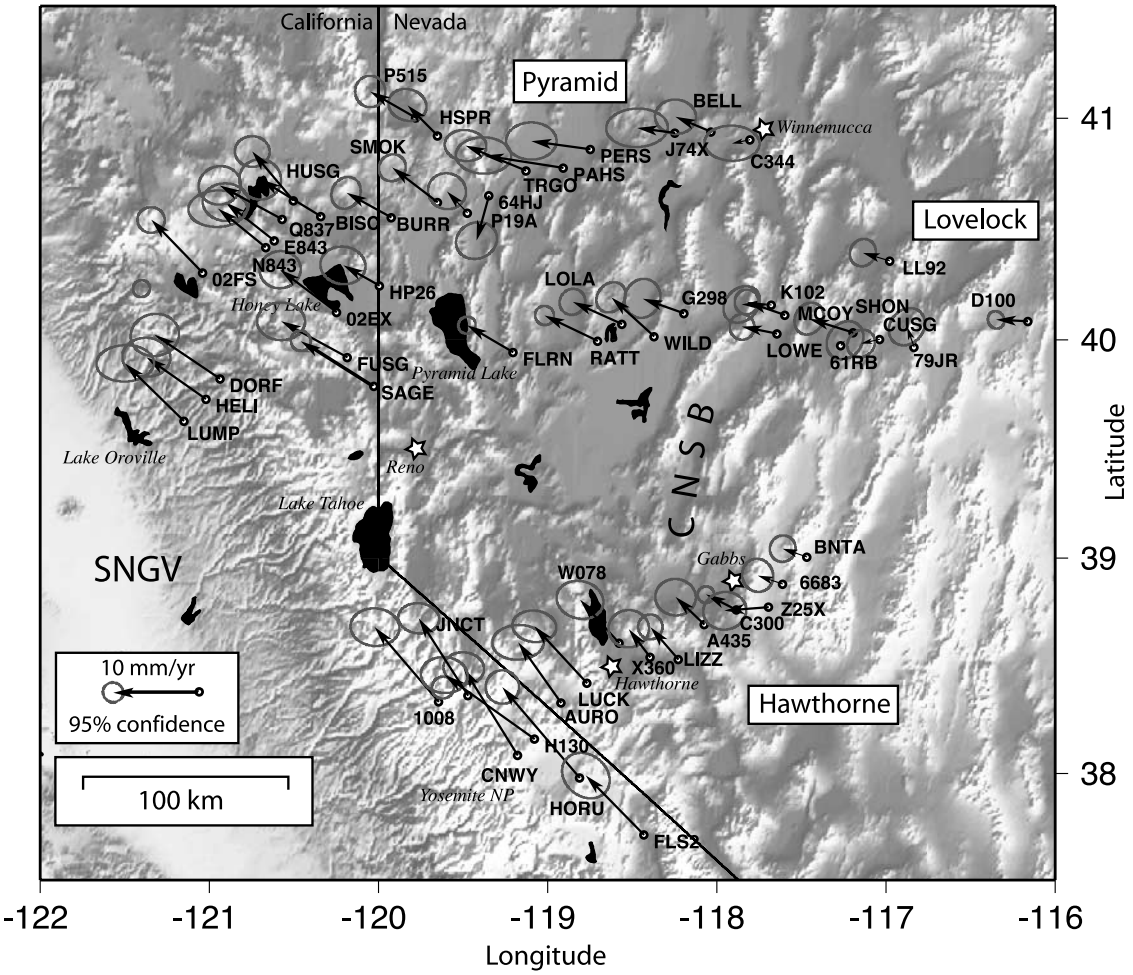


**Figure 1.** New velocities obtained from surveys of the 2000 and 2004 Pyramid, Lovelock, and Hawthorne networks of the western Basin and Range province. Velocities are in the Stable North America Reference Frame (SNARF). Ellipses are the 95% confidence uncertainties. Location of central Nevada Seismic Belt (CNSB) is shown near the location of the Dixie Valley and Fairview Peak earthquakes.

carrier phase and pseudorange were processed every 5 min. Estimated parameters included a tropospheric zenith bias and two gradient parameters estimated as random walk processes, and station clock corrections estimated as a white noise process.

[9] Before velocities are computed, regional filtering was applied to the position time series so that the effects of daily common mode perturbations in the reference frame can be reduced. Regional filtering tends to reduce the RMS residual scatter of time series and improve the consistency of rates inside a regional network of sites [*Wdowinski et al.*, 1997; *Dong et al.*, 1998]. It was assumed that each site moves with a constant velocity, and that shifts in the entire network that do not deform the polygons defined by the sites are attributed to reference frame noise. For each day a transformation is applied that minimizes the misfit between a selected set of spatially well-distributed continuous sites and their expected position. The selected sites are required to be the longest running and most stable sites in the network (CMBB, DYER, GABB, RAIL, MINE, TUNG, SUTB, GARL, SHLD, YBHB, QUIN). The expected position is based on the velocity of the site, determined via least squares estimation, before the filtering is applied. In this case the transformation consisted of 3 rotation parameters with coordinate origin fixed to the geocenter. Thus the transformation took account of horizontal positions only so that any unaccounted effects of campaign reoccupation on the vertical position would not affect the results of the filtering. After the filtering, new rates are determined and the process is repeated, iterating until velocities do not change significantly. At each iteration outliers are identified as those positions >10 standard deviations away from the expected position, and removed. Convergence occurs after three iterations. Regional filtering and outlier removal from the position time series reduces the total RMS noise (including campaign and continuous sites) by ~32%.

[10] We further excluded data with limited occupation histories and where it was impossible to reliably identify outliers or adequately estimate uncertainties. We excluded all sites that had two or fewer measurements. We also

**Table 1.** Velocities in SNARF North America Reference Frame

| Site | Longitude | Latitude | Ve | Vn | $\sigma_e$ | $\sigma_n$ |
|---|---|---|---|---|---|---|
| | | | *Campaign Sites* | | | |
| Pyramid | | | | | | |
| 02EX | −120.25 | 40.13 | −6.72 | 5.04 | 0.99 | 0.90 |
| 02FS | −121.04 | 40.30 | −6.06 | 6.27 | 0.66 | 0.62 |
| 64HJ | −119.35 | 40.65 | −1.48 | −5.35 | 0.99 | 0.89 |
| BELL | −118.03 | 40.94 | −4.24 | 1.78 | 0.99 | 0.83 |
| BISC | −120.34 | 40.56 | −7.17 | 4.38 | 1.01 | 0.97 |
| BURR | −119.92 | 40.55 | −5.34 | 2.94 | 0.71 | 0.77 |
| C344 | −117.80 | 40.91 | −2.14 | −0.45 | 1.33 | 0.85 |
| DORF | −120.94 | 39.82 | −7.72 | 5.20 | 1.17 | 1.02 |
| E843 | −120.61 | 40.45 | −5.75 | 4.52 | 1.12 | 0.91 |
| FUSG | −120.18 | 39.92 | −7.86 | 4.28 | 1.16 | 0.91 |
| HELI | −121.02 | 39.73 | −7.06 | 4.96 | 1.16 | 0.94 |
| HP26 | −119.99 | 40.24 | −4.32 | 2.43 | 1.09 | 0.91 |
| HSPR | −119.65 | 40.92 | −3.59 | 3.62 | 0.92 | 0.77 |
| HUSG | −120.50 | 40.63 | −4.87 | 5.81 | 0.84 | 0.74 |
| J74X | −118.25 | 40.94 | −4.52 | 0.59 | 1.49 | 0.93 |
| LUMP | −121.15 | 39.63 | −6.96 | 6.81 | 1.39 | 0.88 |
| N843 | −120.67 | 40.42 | −5.65 | 4.60 | 1.42 | 0.88 |
| P19A | −119.47 | 40.58 | −2.45 | 2.56 | 0.92 | 0.87 |
| P515 | −119.78 | 41.00 | −5.40 | 3.09 | 0.73 | 0.76 |
| PAHS | −118.91 | 40.78 | −9.45 | 1.47 | 1.34 | 0.88 |
| PERS | −118.75 | 40.86 | −7.03 | 0.96 | 1.22 | 0.90 |
| Q837 | −120.57 | 40.55 | −7.37 | 3.98 | 1.02 | 0.93 |
| SAGE | −120.04 | 39.79 | −8.42 | 5.32 | 0.48 | 0.49 |
| SMOK | −119.65 | 40.62 | −5.38 | 4.11 | 0.65 | 0.65 |
| TRGO | −119.13 | 40.77 | −7.19 | 2.97 | 1.01 | 0.75 |
| Lovelock | | | | | | |
| 61RB | −117.27 | 39.98 | 0.47 | 0.59 | 0.89 | 0.92 |
| 79JR | −116.83 | 39.97 | −0.85 | 2.40 | 0.87 | 0.90 |
| CUSG | −117.04 | 40.00 | −2.22 | −0.50 | 0.67 | 0.67 |
| D100 | −116.16 | 40.08 | −3.77 | 0.19 | 0.40 | 0.42 |
| FLRN | −119.20 | 39.94 | −5.49 | 3.21 | 0.42 | 0.41 |
| G298 | −118.19 | 40.12 | −4.92 | 1.74 | 0.87 | 0.94 |
| K102 | −117.68 | 40.16 | −3.51 | 0.05 | 0.88 | 0.88 |
| LL92 | −116.98 | 40.36 | −3.21 | 0.95 | 0.63 | 0.66 |
| LOLA | −118.56 | 40.07 | −5.86 | 2.64 | 0.62 | 0.63 |
| LOWE | −117.64 | 40.03 | −4.16 | 0.83 | 0.60 | 0.62 |
| MCOY | −117.60 | 40.11 | −4.55 | 1.57 | 0.58 | 0.60 |
| RATT | −118.70 | 40.00 | −6.30 | 3.01 | 0.46 | 0.46 |
| SHON | −117.19 | 40.03 | −5.25 | 1.62 | 0.71 | 0.77 |
| WILD | −118.37 | 40.02 | −5.09 | 4.64 | 0.71 | 0.73 |
| Hawthorne | | | | | | |
| 1008 | −119.64 | 38.33 | −7.58 | 8.83 | 1.18 | 0.91 |
| 6683 | −117.61 | 38.88 | −2.98 | 1.00 | 0.75 | 0.80 |
| A435 | −118.07 | 38.69 | −3.40 | 3.26 | 0.98 | 0.88 |
| AURO | −118.92 | 38.33 | −5.10 | 7.20 | 1.25 | 0.84 |
| BNTA | −117.47 | 39.01 | −2.88 | 0.97 | 0.62 | 0.64 |
| C300 | −117.88 | 38.76 | −3.61 | 1.84 | 0.40 | 0.40 |
| CNWY | −119.18 | 38.08 | −6.41 | 10.32 | 0.98 | 0.77 |
| FLS2 | −118.43 | 37.71 | −6.90 | 7.04 | 1.15 | 1.10 |
| H130 | −119.08 | 38.16 | −10.66 | 7.59 | 1.13 | 0.87 |
| HORU | −118.81 | 37.98 | −9.17 | 10.75 | 0.81 | 0.81 |
| JNCT | −119.47 | 38.36 | −5.87 | 9.18 | 0.99 | 0.73 |
| LIZZ | −118.23 | 38.53 | −3.32 | 3.84 | 0.59 | 0.60 |
| LUCK | −118.77 | 38.42 | −6.26 | 6.76 | 1.06 | 0.76 |
| W078 | −118.58 | 38.61 | −4.64 | 5.15 | 1.13 | 0.92 |
| X360 | −118.39 | 38.54 | −2.56 | 3.35 | 0.98 | 0.90 |
| Z25X | −117.69 | 38.77 | −5.23 | −0.41 | 1.04 | 0.91 |
| | | | *Continuous Sites* | | | |
| NBAR | | | | | | |
| BAMO | −117.20 | 40.41 | −4.26 | 2.02 | 0.62 | 0.62 |
| CAST | −110.68 | 39.19 | −1.00 | 0.76 | 0.39 | 0.39 |
| CEDA | −112.86 | 40.68 | −3.37 | −0.11 | 0.39 | 0.39 |
| COON | −112.12 | 40.65 | −2.52 | −0.04 | 0.39 | 0.39 |
| EGAN | −114.94 | 39.35 | −3.01 | 0.09 | 0.39 | 0.39 |
| ELKO | -115.82 | 40.91 | −4.18 | 0.62 | 0.39 | 0.39 |
| FOOT | −113.81 | 39.37 | −3.41 | 0.29 | 0.39 | 0.39 |
| GABB | −117.92 | 38.97 | −3.98 | 1.88 | 0.39 | 0.39 |
| GARL | −119.36 | 40.42 | −5.13 | 3.21 | 0.39 | 0.39 |
| GOSH | −114.18 | 40.64 | −3.55 | 0.15 | 0.39 | 0.39 |
| HEBE | −111.37 | 40.51 | −0.90 | 0.56 | 0.39 | 0.39 |
| LEWI | −116.86 | 40.40 | −2.66 | −0.25 | 0.39 | 0.39 |
| MINE | −116.10 | 40.15 | −2.26 | 0.38 | 0.39 | 0.39 |
| MONI | −116.72 | 39.15 | −3.48 | 0.82 | 0.39 | 0.39 |
| NEWS | −117.51 | 39.69 | −3.82 | 1.14 | 0.39 | 0.39 |
| RUBY | −115.12 | 40.62 | −3.56 | 0.14 | 0.39 | 0.39 |
| SHIN | −120.23 | 40.59 | −6.58 | 4.75 | 0.39 | 0.39 |
| SLID | −119.88 | 39.31 | −8.49 | 7.11 | 0.39 | 0.39 |
| SMEL | −112.84 | 39.43 | −3.00 | 0.29 | 0.39 | 0.39 |
| TUNG | −118.26 | 40.40 | −5.18 | 2.39 | 0.39 | 0.39 |
| UPSA | −118.80 | 39.63 | −6.37 | 3.68 | 0.39 | 0.39 |
| SBAR | | | | | | |
| DYER | −118.04 | 37.74 | −5.18 | 3.57 | 0.42 | 0.42 |
| RAIL | −115.66 | 38.28 | −4.00 | 0.38 | 0.42 | 0.42 |
| TONO | −117.18 | 38.10 | −4.22 | 1.32 | 0.42 | 0.42 |
| BARD | | | | | | |
| CHO1 | −121.66 | 39.43 | −10.50 | 7.68 | 0.41 | 0.41 |
| CMBB | −120.39 | 38.03 | −10.45 | 8.61 | 0.41 | 0.41 |
| DECH | −119.09 | 38.05 | −10.57 | 8.86 | 0.53 | 0.53 |
| MUSB | −119.31 | 37.17 | −10.62 | 9.59 | 0.41 | 0.41 |
| ORVB | −121.50 | 39.55 | −10.23 | 7.39 | 0.41 | 0.41 |
| QUIN | −120.94 | 39.97 | −9.14 | 6.73 | 0.41 | 0.41 |
| SUTB | −121.82 | 39.21 | −10.84 | 7.29 | 0.41 | 0.41 |
| YBHB | −122.71 | 41.73 | −3.03 | 7.27 | 0.41 | 0.41 |
| PANGA | | | | | | |
| SHLD | −119.02 | 41.87 | −3.61 | 2.79 | 0.41 | 0.41 |

eliminated sites that had three or more measurements that occurred in two separate years and one of those years had only a single measurement. In all, 252 velocities were obtained and used in our deformation analysis, 51 of which are sites with previously unpublished campaign site velocities (Figure 1).

[11] Following the filtering, the velocities that were computed in ITRF2000 are placed into a reference frame that is most appropriate for their tectonic interpretation. We have chosen to use the Stable North America Reference Frame (SNARF) [*Blewitt et al.*, 2005] because it is designed specifically for this purpose and accounts for postglacial rebound affecting the otherwise rigid North American craton. The SNARF Euler vector describes the rotation of stable North America with respect to the ITRF2000 reference frame (x = 0.0223, y = −0.1981, z = −0.0083 in degrees per million years). Velocities relative to SNARF for both the 2000–2004 network shown in Figure 1 and nearby continuous and USGS campaign sites are shown in Figures 1–3.

### 2.2. Velocity Uncertainties

[12] Uncertainties in GPS-derived rates of motion are a function of the uncertainty in the positions, the length of the time series, the number of data, the presence of steps in the time series [*Williams*, 2003a] and the noise model assumed [*Agnew*, 1992; *Mao et al.*, 1999; *Williams*, 2003b]. The presence of colored noise represents a particular challenge in estimating the rates of motion of campaign GPS sites because it is not possible to evaluate the power law noise spectra of very sparsely and irregularly sampled data. In the continuous sites that we consider we assume that no steps exist in the time series. In some cases, equipment changes occurred which did not create a noticeable step in the time series. No corrections

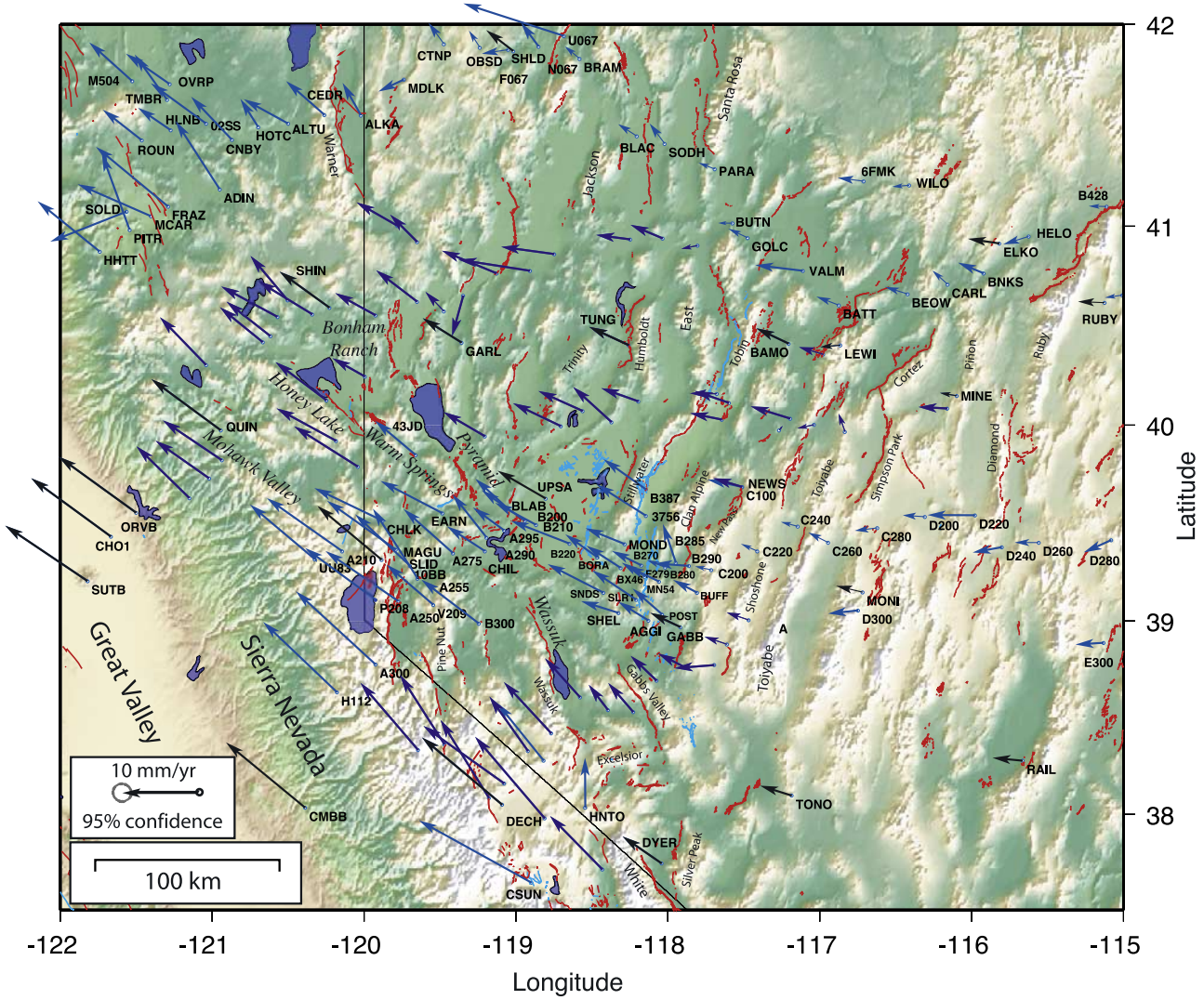


**Figure 2.** Velocities with respect to stable North America for all the sites considered in this study. Vectors indicate new velocities (blue), continuous sites (black), and other USGS campaign sites in the region (light blue). Sinuous colored line segments show historic (cyan) and Holocene (red) surface ruptures. Horizontal text gives the names of sites not shown in Figure 1. Italics denote faults discussed in the text. Remaining nonhorizontal text shows the names of some notable mountain ranges.

were made for these occurrences, although we cannot rule out the possibility that small steps below the noise level of the data could be present. We assumed that the additional velocity uncertainty was attributable to a random walk component of noise, with amplitude 1 mm/$T^{1/2}$ [*Langbein and Johnson*, 1997], where $T$ is the time in years between the first and last observation in the time series. Some studies have found that for the monuments used here, the random walk component of the noise can have a magnitude 2 to 3 times as large as we have assumed [*Williams et al.*, 2004]. However, an analysis of residuals discussed below suggests that our estimate of uncertainties is appropriate. Since no time series are shorter than 4 years long, we did not add a component of noise associated with the presence of unmodeled annual signals, because the bias associated with this effect would be less than 0.2 mm/yr [*Blewitt and Lavallée*, 2002].

[13] To evaluate the size of the velocity uncertainties with respect to potential signal, we inspect two measures of misfit between data and our model. First, for each site $j$, we calculate the misfit between the north $n_{obs}$ and east $e_{obs}$ position components from the filtered GPS horizontal time series and the position predictions $n_{pred}$ and $e_{pred}$ of a constant velocity model

$$\chi^2_{vel,j} = \frac{1}{p}\left\{\sum_{i=1}^{M_j}\left[\frac{(n_{obs,i}-n_{pred,i})}{\sigma_{n,i}}\right]^2 + \sum_{i=1}^{M_j}\left[\frac{(e_{obs,i}-e_{pred,i})}{\sigma_{e,i}}\right]^2\right\} \quad (1)$$

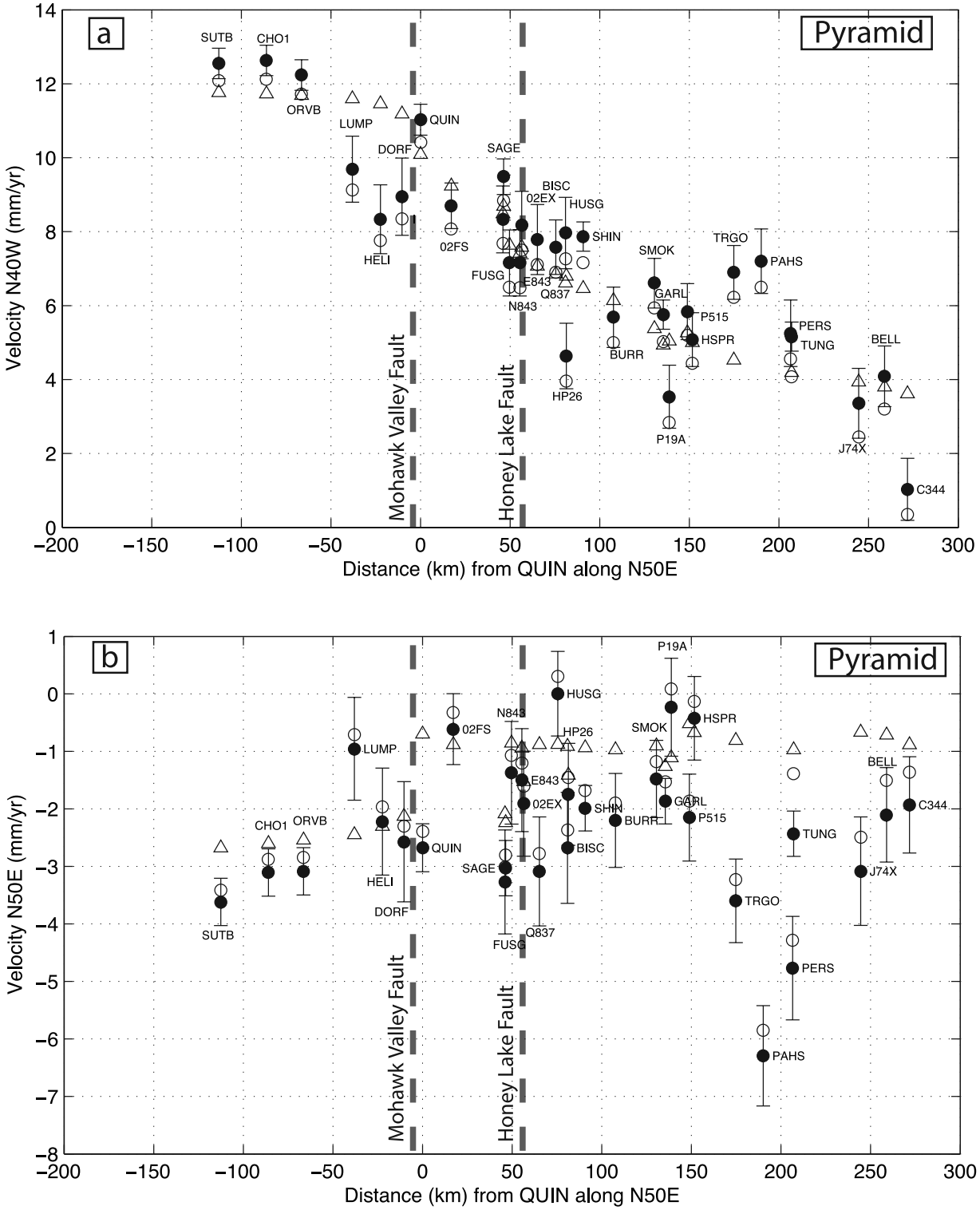


**Figure 3.** (a) N40°W component of velocities with respect to stable North America for the Pyramid profile, as a function distance from the site QUIN measured in the direction N50°E. (b) Same as Figure 3a but for N50°E component of velocity. (c) N60°W component of velocities with respect to stable North America for the Lovelock profile, as a function distance from the site LOLA measured in the direction N60°W. (d) Same as Figure 3c but for N30°E component of velocity. (e) N35°W component of velocities with respect to stable North America for the Hawthorne profile, as a function distance from the site GABB measured in the direction N55°E. (f) Same as Figure 3e but for N55°E component of velocity. Black circles are GPS velocity results with 2-sigma uncertainty bars, open circles indicate the GPS velocities adjusted for postseismic relaxation using the model of *Hammond et al.* [2007], open triangles indicate the velocity predicted from the block model shown in Figure 8.

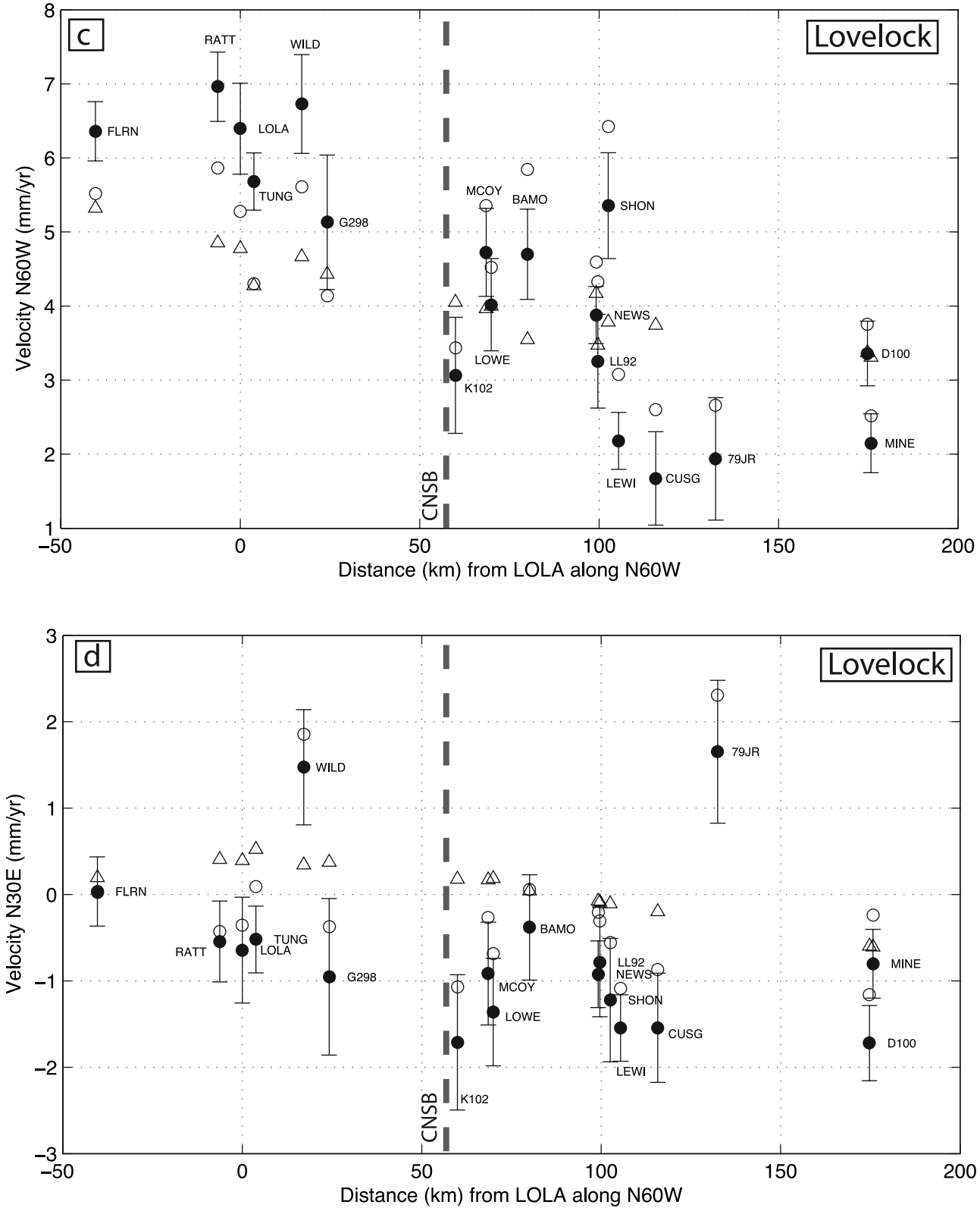


**Figure 3.** (continued)

where $p$ is the number of degrees of freedom in the problem, which is equal to the number of data (two times the number of times with positions $M_j$) minus the number of free parameters (4, a rate and an intercept for each horizontal coordinate). The uncertainties $\sigma_{n,i}$ and $\sigma_{e,i}$ in positions are the formal uncertainties obtained from the GIPSY processing. The resulting misfits have mean $\chi_{vel}^2 = 1.79$ suggesting that either the position uncertainties

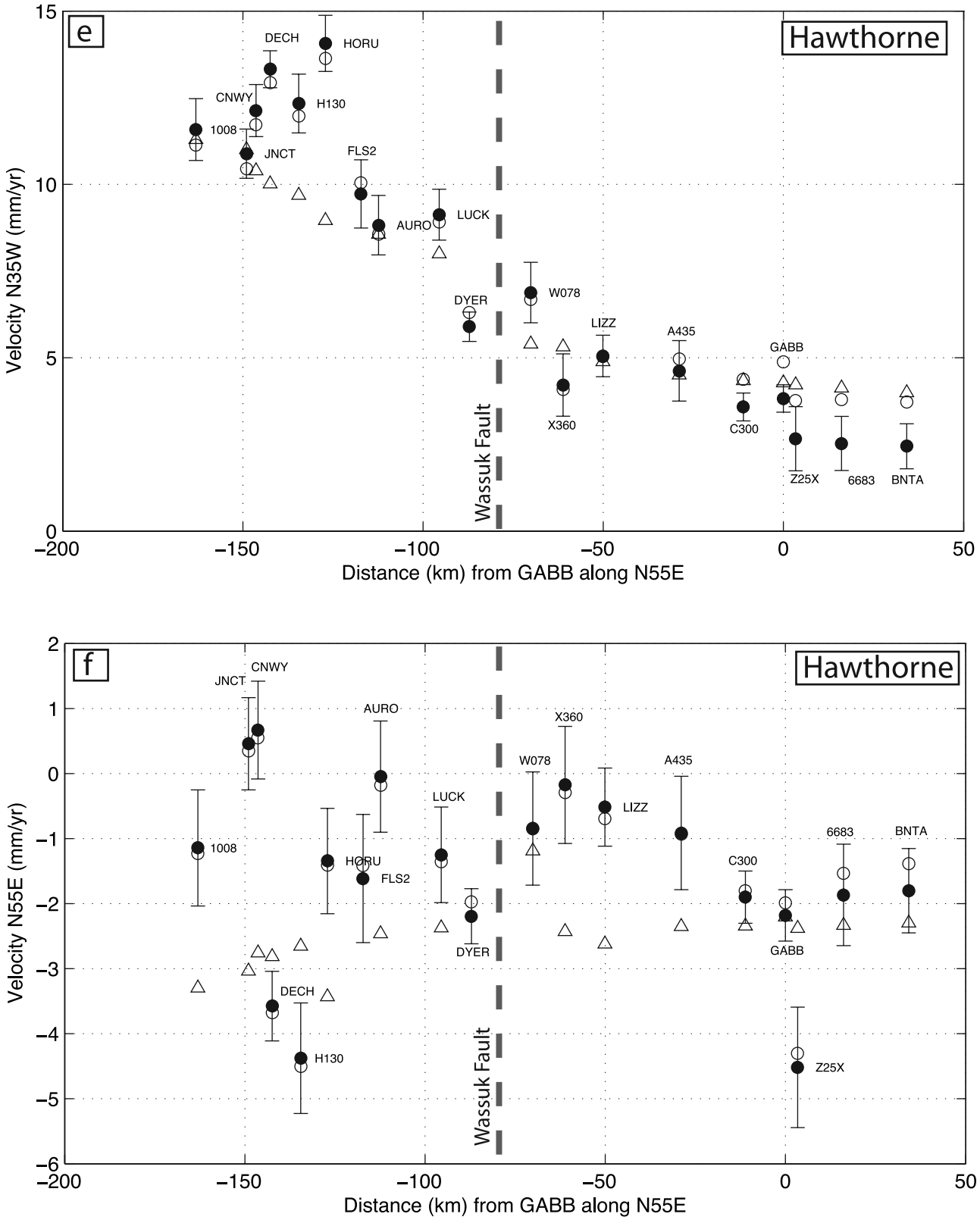


**Figure 3.** (continued)

should be increased by factor of ∼1.34 or that a constant velocity model is too simple to represent the GPS time series. For example, annual, quadratic or other signals in the time series may remain after the common mode part of such signals is removed by the filtering. In this analysis we are concerned with time-invariant rates so we elect to increase the white noise position uncertainties by 1.34 so that the velocity uncertainties include error in the

**Table 2.** Strain Rates Inside Selected Subregions of Our Study Area[a]

| | $\varepsilon_1$ | $\varepsilon_2$ | $\varepsilon_{xy}$ | $\varepsilon_\Delta$ | $\omega$ | $\alpha$ | N |
|---|---|---|---|---|---|---|---|
| | | | *Pyramid* | | | | |
| Mean | 12.6 ± 1.0 | −9.7 ± 1.0 | 22.4 ± 1.4 | 2.9 ± 1.4 | 15.7 ± 0.6 | −86 ± 2 | 84 |
| Max (near 120°W) | 23.7 ± 2.6 | −15.8 ± 1.5 | 39.0 ± 3.0 | 7.9 ± 3.0 | 24.6 ± 1.4 | −83 ± 3 | 48 |
| East End (near 118.1°W) | 9.8 ± 4.8 | −0.4 ± 3.6 | 10.2 ± 6.0 | 9.4 ± 6.0 | 11.4 ± 3.0 | −94 ± 17 | 24 |
| West Half | 11.8 ± 2.1 | −15.9 ± 2.2 | 27.7 ± 3.0 | −4.1 ± 3.0 | 19.0 ± 1.6 | −101 ± 5 | 33 |
| | | | *Lovelock* | | | | |
| Mean | 9.9 ± 0.7 | −8.7 ± 0.9 | 18.6 ± 1.1 | 1.1 ± 1.1 | 8.6 ± 0.6 | −71 ± 2 | 112 |
| West End | 17.4 ± 3.1 | −14.4 ± 2.1 | 31.8 ± 3.8 | 2.9 ± 3.8 | 11.8 ± 1.9 | −84 ± 4 | 41 |
| West Half (west of 117°W) | 20.4 ± 1.1 | −11.3 ± 1.2 | 31.7 ± 1.6 | 9.0 ± 1.6 | 12.1 ± 0.8 | −73 ± 1 | 82 |
| Near 118.5°W | 31.7 ± 2.7 | −8.4 ± 2.7 | 40.1 ± 3.8 | 23.3 ± 3.8 | 5.5 ± 1.9 | −65 ± 2 | 38 |
| West Half relaxation corrected | 13.8 ± 1.1 | −10.6 ± 1.2 | 24.4 ± 1.7 | 3.2 ± 1.7 | 10.2 ± 0.8 | −80 ± 2 | 82 |
| East Half (east of 117°W) | 0.8 ± 1.6 | −2.0 ± 1.9 | 2.8 ± 2.5 | −1.1 ± 2.5 | 4.4 ± 1.2 | 179 ± 30 | 30 |
| East half relaxation corrected | 0.2 ± 1.6 | −1.0 ± 1.9 | 1.2 ± 2.5 | −0.9 ± 2.5 | 6.1 ± 1.2 | 160 ± 44 | 30 |
| | | | *Hawthorne* | | | | |
| Mean | 24.8 ± 1.4 | −23.0 ± 1.8 | 47.8 ± 2.3 | 1.8 ± 2.3 | 22.4 ± 1.3 | −79 ± 2 | 58 |
| Upper Transect Maximum | 48.8 ± 4.5 | −33.7 ± 3.1 | 82.5 ± 5.4 | 15.2 ± 5.4 | 35.5 ± 2.7 | −82 ± 2 | 27 |
| Lower Transect Maximum | 46.2 ± 4.4 | −34.4 ± 2.8 | 80.6 ± 5.2 | 11.7 ± 5.2 | 35.0 ± 2.5 | −81 ± 2 | 28 |
| Upper Transect (near 118°W) | 44.8 ± 9.1 | −11.0 ± 8.6 | 55.7 ± 12.5 | 33.8 ± 12.5 | 30.0 ± 6.4 | −77 ± 6 | 21 |
| Upper Transect (near 118°W) relaxation corrected | 27.0 ± 9.1 | −5.7 ± 8.6 | 32.6 ± 12.5 | 21.3 ± 12.5 | 19.6 ± 6.4 | −89 ± 12 | 21 |
| Western Great Basin (longitude <116°W, latitude <42°N) | 14.3 ± 0.6 | −11.8 ± 0.6 | 26.1 ± 0.8 | 2.6 ± 0.8 | 14.3 ± 0.4 | −80 ± 1 | 150 |
| NW Nevada (120°W to 116°W, 39°N to 43°N) | 12.0 ± 0.8 | −8.3 ± 0.7 | 20.3 ± 1.1 | 3.7 ± 1.1 | 11.9 ± 0.5 | −78 ± 2 | 101 |
| Dilatation Zone (119°W to 117°W, 39° to 40.5°) | 31.4 ± 2.8 | −8.3 ± 2.6 | 39.7 ± 3.9 | 23.0 ± 3.9 | 7.1 ± 1.8 | −66 ± 2 | 39 |
| Dilatation Zone, relaxation corrected | 13.5 ± 2.8 | −6.5 ± 2.6 | 20.0 ± 3.9 | 6.9 ± 3.9 | 3.3 ± 1.8 | −76 ± 5 | 39 |

[a]Uncertainties are 1 standard deviation, $\varepsilon_\Delta = \varepsilon_1 + \varepsilon_2$, $\varepsilon_{xy} = \varepsilon_1 - \varepsilon_2$; $\omega$ is rotation rate; $\alpha$ is direction of maximum extension in degrees clockwise from north; N is number of sites used in tensor strain rate estimation.

assumption of a constant velocity. Second, we chose the subset of sites between longitude 113°W and 117°W, where several studies have shown the central Basin and Range to be nearly nondeforming [*Bennett et al.*, 1998; *Thatcher et al.*, 1999; *Bennett et al.*, 2003; *Hammond and Thatcher*, 2004, 2005]. For these sites we calculated the mean motion and horizontal strain rate on a sphere (3 horizontal strain rate and 3 Euler rotation parameters) [*Savage et al.*, 2001]. In agreement with previous results, the average strain rate in this region is not significantly different than zero (although see discussion in section 4.4). The misfit between the predictions of north and east velocity from this model ($vn_{\mathrm{mod}}$ and $ve_{\mathrm{mod}}$, respectively) and the velocities obtained from the GPS time series ($vn_{\mathrm{obs}}$ and $ve_{\mathrm{obs}}$) data is

$$\chi^2_{strain} = \frac{1}{q}\left\{\sum_{k=1}^{N}\left[\frac{\left(vn_{obs,k} - vn_{pred,k}\right)}{\sigma_{vn,k}}\right]^2 + \sum_{k=1}^{N}\left[\frac{\left(ve_{obs,k} - ve_{pred,k}\right)}{\sigma_{ve,k}}\right]^2\right\} \quad (2)$$

where $q$ is the strain problem degrees of freedom, which is equal to the number of velocities (two components per site equals 74) minus the number of free parameters (3 strain + 3 rotation = 6). The uncertainties in velocity $\sigma_{vn}$ and $\sigma_{ve}$ are those obtained from least squares regression (with position uncertainties already increased by factor of 1.34) and augmented by random walk noise. The results is that $\chi^2_{strain}$ = 1.91, suggesting that our uncertainties should be again increased by a factor of 1.38 or that there is more structure in the velocity field that is described by a constant strain rate model. We choose not to increase the velocity uncertainties further, since deviation from a constant strain rate is a possibility. For campaign sites, mean 1-sigma uncertainty in the east (north) velocity are 0.91 (0.78) mm/yr and for continuous sites are 0.43 (0.43) mm/yr.

## 3. Results

[14] The velocities and uncertainties obtained in this study are shown in Tables 1 and S1 and plotted in Figures 1–3. For each of the profiles we calculated an average strain rate (Table 2), including the velocities for continuous sites and other USGS campaigns in the immediate vicinity. For display purposes, we use this average strain rate to define a preferred direction in which to rotate the horizontal coordinate axes (Figure 3). In the Pyramid network, deformation is predominantly shear in the direction N40°W, in the Lovelock network the deformation is a combination of shear and extension with maximum extension in the direction N60°W, and in the Hawthorne network deformation is predominantly shear in the direction N35°W. The spatially varying strain calculations described below, and shown in Figures 4, 5, and 6, use all of the velocities shown in Figure 2. Inclusion of all the velocities often permits us to uniquely resolve deformation and rotation parameters that otherwise would be poorly constrained. For example, if we consider only sites from the quasi-linear Pyramid network it is difficult to uniquely distinguish shear deformation from rotation. By adding sites from the Lassen network to the north, some sites from western Nevada, the Highway 50 network to the south, and other nearby continuous sites, the network is strong enough to independently resolve shear and rigid rotation, albeit at the cost of averaging these parameters over larger areas. We define shear as the difference between the horizontal principal strain rates $\varepsilon_{xy} = \varepsilon_1 - \varepsilon_2$, and

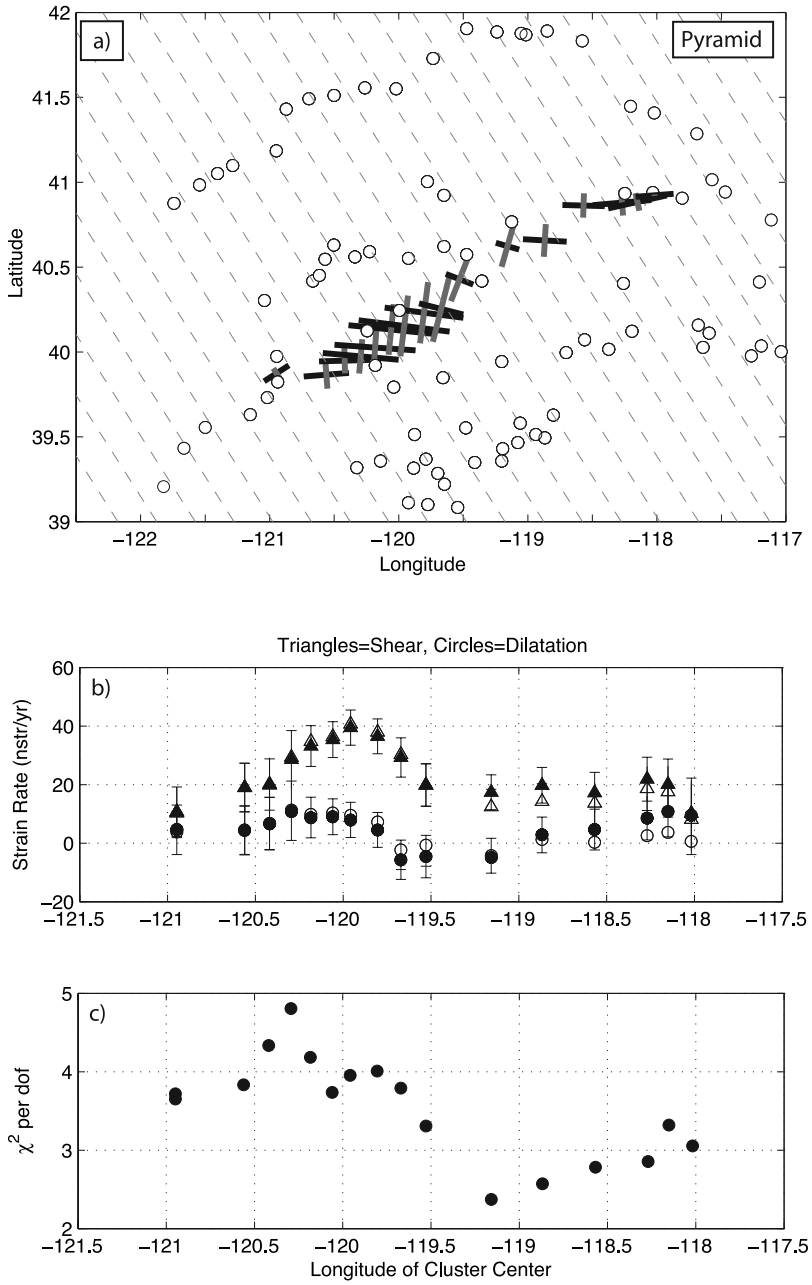


**Figure 4.** Transitions in deformation inferred across the Pyramid network. (a) Circles represent all GPS sites used in the calculation of tensor strain rates which are indicated with orthogonal black (extension) and gray (contraction) bars. Dashed lines are oriented parallel to the N40°W direction of maximum shear across the network. The tensor strain scale is the same in Figures 4a, 5a, and 6a. (b) Shear (triangles) and dilatational (circles) deformation at the centroid of each subnetwork used to obtain strain rate tensors. Note that uniaxial extension occurs when shear ($\varepsilon_1 - \varepsilon_2$) and dilatation ($\varepsilon_1 + \varepsilon_2$) are equal. Error bars show 2-sigma uncertainties. Strain is given in $10^{-9}$/yr. Open symbols indicate strain rates obtained from velocities adjusted using the postseismic relaxation model of *Hammond et al.* [2007]. (c) The $\chi^2$ misfit for each strain rate estimate.

dilatation as the sum of principal strains $\varepsilon_\Delta = \varepsilon_1 + \varepsilon_2$, where extension is reckoned positive.

[15] To characterize the spatial variations in the velocity and deformation fields, we calculated the strain rates inside subsets of sites along each network. Subsets of sites are bounded by two parallel lines, 200 km apart, oriented parallel to the average direction of shear or extension for each network as described above. The width of this band was chosen to be wide enough to include enough sites (13–40) in each subset, but narrow enough to reveal variations in the first-order deformation characteristics. This 200-km-wide band is translated along the network, capturing successive subsets of sites within which the tensor strain rate is calculated using the method of *Savage et al.* [2001]. This

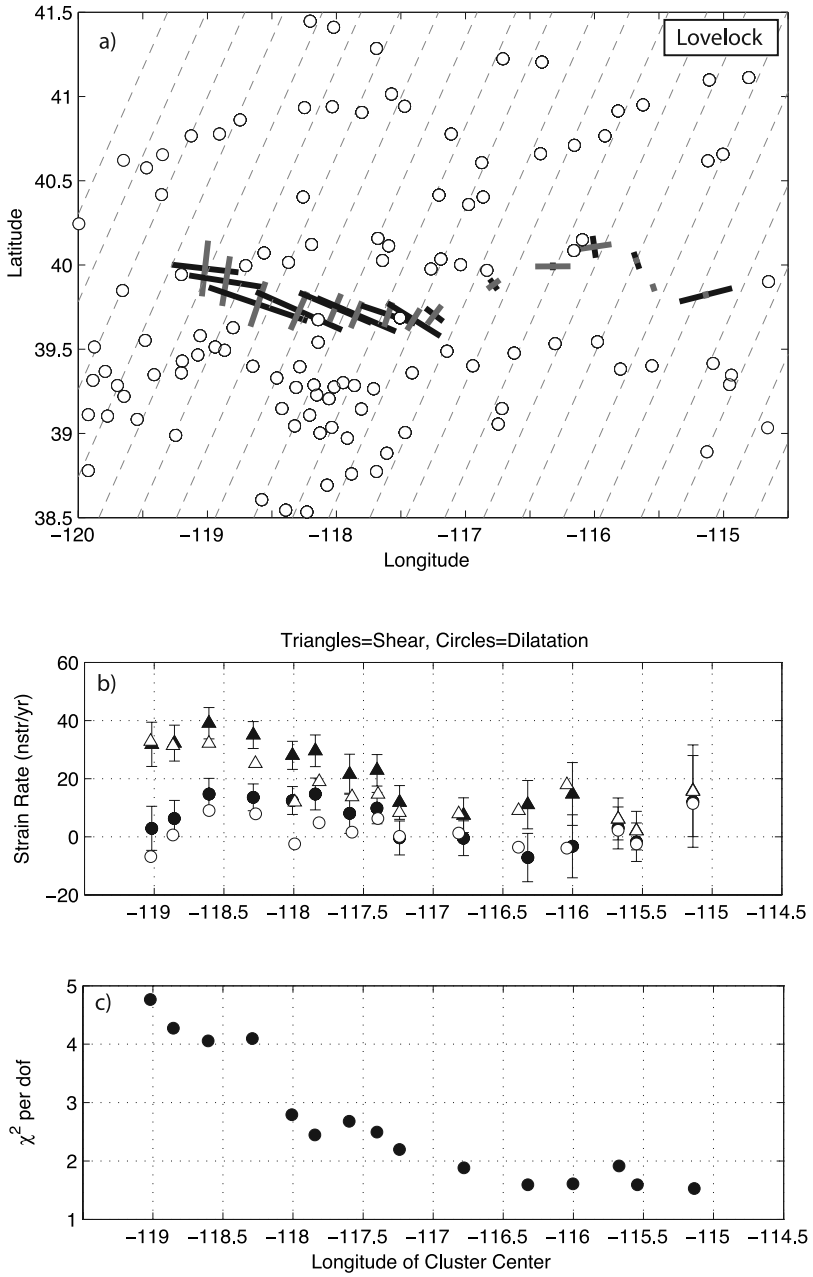


**Figure 5.** Transitions in deformation inferred across the Lovelock network. Symbols are the same as in Figure 4. Dashed lines are oriented parallel to the N60°W direction of maximum extension across the network.

moving window analysis results in substantial overlap of sites and produces strain rate fields (Figures 4–6) that are spatially smoothed. First-order transitions in the intensity and style of the strain rates fields are, however, clearly detected. In all cases careful attention was paid to effects of any velocity outliers on the strain rate determinations. In some cases particular velocities were deleted, because they were either obvious outliers, or were contaminated by known groundwater extraction effects unrelated to tectonic deformation (specific sites are noted in sections below).

### 3.1. Pyramid Profile

[16] For the Pyramid network we include continuous and campaign sites in networks adjacent to the Pyramid profile, e.g., the Lassen line to the north [*Hammond and Thatcher*, 2005], and the other nearby networks to the south. This includes sites in the Highway 50 network [*Thatcher et al.*, 1999; *Hammond and Thatcher*, 2004], western Nevada networks [*Svarc et al.*, 2002], and the Lassen line [*Hammond and Thatcher*, 2005] inside the box bounded by longitude 122.5°W to 117°W, and latitude 39°N to 42°N. The sites SOLD, U067, and 64HJ were omitted because their velocities appear to be outliers, and we omitted the sites around the Medicine Lake volcanic

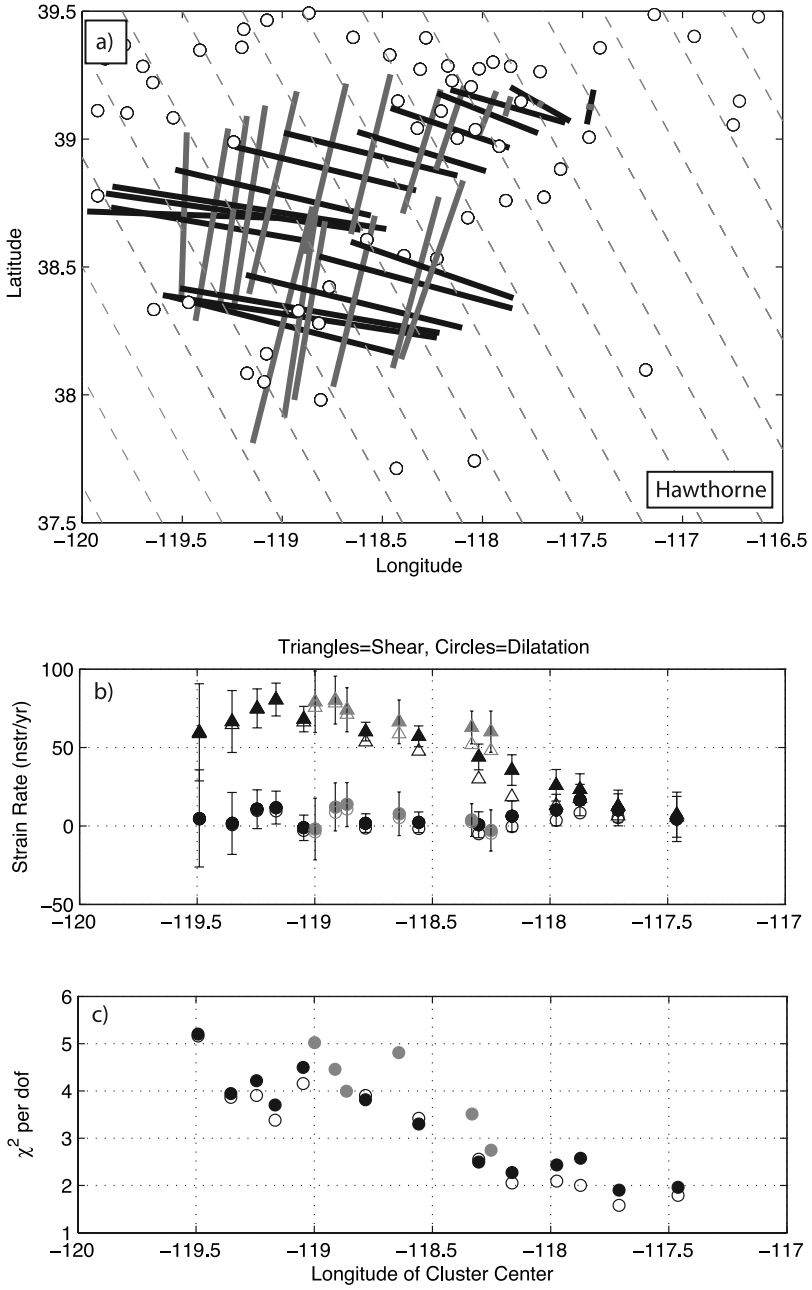


**Figure 6.** Transitions in deformation inferred across the Hawthorne network. Symbols are the same as in Figures 4 and 5, except that gray symbols in Figure 6b indicate the strain rates inferred from subsets of the velocities below 39°N latitude. Dashed lines are oriented parallel to the N35°W direction of maximum shear across the network.

zone (M504, OVRP, TMBR, ROUN, HLNB, 02SS), which is affected by a subsurface deflationary source related to magmatic activity [*Dzurisin et al.*, 2002]. Sites that are far from the Pyramid network (i.e., sites both east of 118.7°W and south of 39.7°N, lower right corner of Figure 4a) were omitted from the strain analysis discussed below since they likely have a different strain pattern than exists along the Pyramid profile [e.g., *Svarc et al.*, 2002; *Hammond and Thatcher*, 2004].

[17] In total, approximately 11 mm/yr of relative motion occurs across this zone (Figure 3a), roughly equal to the entire budget of shear deformation between the Sierra Nevada microplate and the central Basin and Range [*Thatcher et al.*, 1999; *Bennett et al.*, 2003]. There is also considerable (~3–4 mm/yr) scatter in the component of velocity along the N50°E direction, normal to the shear direction. The sites PERS and PAHS apparently move anomalously rapidly in the direction N50°E by between 1 and 4 mm/yr. The average deformation for the entire area shown in Figure 4a is $\varepsilon_{\Delta}$ + 2.9 ± 1.4 nstrain/yr, and $\varepsilon_{xy}$ = 22.4 ± 1.4 nstrain/yr (all quoted uncertainties in this paper are one standard deviation), indicating the Pyramid profile encompasses a zone of right-lateral shear with marginally significant net area growth.

[18] The characteristics of the strain rate field change from east to west across the network (Figures 4a and 4b). The northeast end exhibits significant uniaxial extension of 17.7 ± 4.9 nstrain/yr with the direction of maximum extension oriented N77° ± 8°E. This can be seen in Figure 4b where the shear and dilatation are equal, indicating uniaxial extension ($\varepsilon_1 + \varepsilon_2 = \varepsilon_1 - \varepsilon_2 \Rightarrow \varepsilon_2 = 0$). This extension occurs in northwest Nevada where east-west extension was inferred based on GPS results spanning from northern California to northern Nevada [*Hammond and Thatcher*, 2005]. Removing the arguably anomalous sites PAHS and PERS from the strain calculation (see Figure 2) changes the pattern of strain only marginally: the total uniaxial strain rate near 118.2°W is reduced to 9.8 ± 4.8 nstrain/yr, and the contraction seen near 119.5°W becomes indistinguishable from zero. Farther west, between 118.8°W and 120°W, the style of deformation changes to shear oriented essentially parallel to the N40°W direction of Sierra Nevada motion with respect to the Central Basin and Range [*Dixon et al.*, 2000; *Kreemer et al.*, 2007]. Near 119.5°W, there is some apparently significant contraction that lies between zones of dilatation-free shear near 118.8°W and 119.8°W. At the western end of the network, west of 120.5°W, the shear deformation decreases to near zero with marginally significant uniaxial extension directed N57° ± 5°E. West of 121°W deformation becomes indistinguishable from zero on the SNGV microplate. In general the deformation is less well resolved on the southwest end of the network because the three continuous sites SUTB, CHO1, and ORVB are isolated from other sites that could be used to quantify velocity gradients. Since these sites move rigidly with respect to others to the south they lie on the SNGV microplate [*Dixon et al.*, 2000; *Kreemer et al.*, 2007].

[19] The peak in shear deformation (39.0 ± 3.0 nstrain/yr) occurs at 120°W, 40°N, near where the profile crosses the right-lateral, left-stepping Honey Lake, Warm Springs and Pyramid (HWP) fault system. The shear direction is oriented N38° ± 3°W, approximately parallel to both the average strike of this system and motion of the SNGV relative to the central Basin and Range. This elevated level of shear occurs inside a zone of deformation that is on average approximately half the peak magnitude and spans the entire length of the Pyramid network. The level of misfit of a constant strain rate model is higher where the shear strain rates are greatest (Figure 4c), indicating short-wavelength variations in the strain rate field that may be due to complexities in crustal block structure and/or elastic strain accumulation effects. The elevated strain rates indicate that the HWP fault system is one of the most important shear zones accommodating relative motion between the SNGV and the central Basin and Range. It has been estimated from offsets of volcanic-ash-filled paleovalleys and other geologic data that these faults have a slip rate of 2–10 mm/yr over the last 3–9 million years [*Henry et al.*, 2003; *Faulds et al.*, 2005a]. The western Great Basin budget of ~11 mm/yr and the presence of contemporary deformation across the whole zone appears to rule out the high end of this range for the HWP system. While the HWP system lies in a structural low bounded by normal faults (e.g., the range front fault of the Diamond mountains of the Sierra Nevada), the normal faults show no evidence of Holocene or even Quaternary displacement [*Henry et al.*, 2007], consistent with the dominant present-day shear found in this study.

[20] At the westernmost end of the Pyramid network marginally significant uniaxial extension is inferred ($\varepsilon_1$ = 7.6 ± 3.0 nstrain/yr, and $\varepsilon_2$ is not significant) oriented N123° ± 5°W. This zone, near 121°W, 40°N is not far from the location of the August 1975 Oroville earthquake ($M_b$ 5.9) and subsequent aftershock sequence [*Morrison et al.*, 1976; *Lahr et al.*, 1976; *Savage et al.*, 1977]. The event had a normal faulting mechanism and produced some surface rupture [*Clark et al.*, 1976]. The strike of the fault inferred from seismic data (approximately N3°E, dipping 60° west) is oriented at a high angle to the extension inferred from GPS, possibly suggesting that the observed extension represents a long-lived postseismic transient of the 1975 earthquake. On the other hand, the northeast boundary of the SNGV may be more diffuse than previously appreciated, or low rate deformation is occurring within the northern half of the SNGV, or the extension is an artifact of the relatively poor network geometry at the west end of the Pyramid network.

[21] Velocities adjusted for CNSB postseismic effects according to the model of *Hammond et al.* [2007] (Figure 3) are also used to calculate strain rate values (Figure 4b) for the Pyramid, Lovelock and Hawthorne networks. The adjustment is intended to compensate for transient effects in the observed strain rates, and to estimate the deformation associated with secular (time-invariant) crustal deformation. The open symbols in Figures 4, 5, and 6 indicate the strain rates calculated from the adjusted velocities. In the Pyramid profile the effects of the postseismic adjustment are small. Only east of ~118.5°W does the correction have a noticeable effect on the dilatation, where it is reduced to almost zero. Between 119.2°W and 118.2°W the shear strain is reduced by an amount that is less than the uncertainty in the strain rates.

### 3.2. Lovelock

[22] The Lovelock network occupies a region east of the Walker Lane, in a zone that is more commonly referred to as the central Basin and Range, which deforms much less rapidly than the Walker Lane transtensional zone to the west [*Thatcher et al.*, 1999; *Bennett et al.*, 2003; *Wesnousky et al.*, 2005]. The west half of the Lovelock profile crosses the Central Nevada Seismic Belt (CNSB) near the Stillwater and Tobin ranges (Figure 2), a zone of historic normal and oblique-normal faulting [*Caskey et al.*, 2000]. It has been recognized as a zone of anomalously high geodetic strain rates compared to the east [*Hammond and Thatcher*, 2004], possibly associated with more rapid fault slip rates or enhanced deformation from postseismic deformation [*Savage and Church*, 1974; *Hetland and Hager*, 2003, *Gourmelen and Amelung*, 2005; *Hammond et al.*, 2007].

[23] Similar to our analysis of the Pyramid network, we include sites from networks that run parallel to the Lovelock profile to the north and south. These include sites from the Winnemucca network to the north [*Hammond and Thatcher*, 2005] and also the Highway 50 network to the south [*Thatcher et al.*, 1999; *Hammond and Thatcher*, 2004], and various other USGS campaign sites [e.g., *Svarc et al.*, 2002] and BARGEN continuous sites [*Wernicke et al.*, 2000].

Five sites (64HJ, 61RB, 79JR, B285, Z25X, see Figure 2) exhibit velocities that appear to deviate from the regional pattern and although their effects on the inferred strain patterns were slight, we omitted them from the strain rate calculations. Also the sites PUMP and VALM of the Winnemucca line were omitted since they are affected by subsidence associated with extensive groundwater pumping at nearby mines (J. Bell, personal communication, 2005).

[24] The velocities exhibit an extensional gradient along the preferred direction (N60°W) of 4–5 mm/yr (Figure 3c) between about 117°W to the Trinity range (~118.5°W, Figure 2). The velocities in the N30°E direction vary by less than 2 mm/yr with the exception of WILD and 79JR, which appear to move anomalously rapidly in the N30°E direction by 1–2 mm/yr. Figure 5 shows that transitions in deformation style and intensity occur across the profile. The east half of the network (east of longitude 117°W) experiences no significant deformation. Between 117°W and 118.5°W, in the vicinity of the CNSB, significant shear coexists with significant dilatation that is about half as intense. The dilatational component starts to decrease west of 118.5°W, and finally, at the west end near 119°W, west of the CNSB, the deformation becomes dilatation-free shear across a plane oriented N59° ± 9°W. As was the case for the Pyramid network, the amount of misfit to a constant strain rate model increases when the strain rates are larger (Figure 5c), indicating that the velocity field contains short-wavelength variations not explained by a uniform strain rate field.

[25] The effect of the adjustment for postseismic relaxation is significant near 118.5°W longitude, as would be expected owing to the proximity of the CNSB historic earthquakes (Figure 5b). Both dilatation and shear effects are greater than the uncertainties in the strain rates as far as ~100 km from the CNSB. Beyond this distance the effect is less than the uncertainties. Near the CNSB the adjustment reduces dilatation and shear deformation, and explains nearly all of the dilatation between 118°W and 117°W longitude. Thus it is possible that fault systems directly east of the CNSB (e.g., Clan Alpine to Toiyabe, and Buffalo Valley to Shoshone Fault zones) experience secular strain accumulation that is similar in rate to the central Basin and Range, where the extension rate is below the resolution of previous GPS studies [e.g., *Bennett et al.*, 1998; *Thatcher et al.*, 1999; *Bennett et al.*, 2003; *Hammond and Thatcher*, 2004].

### 3.3. Hawthorne

[26] The Hawthorne profile is a quasi-linear array that traverses the central Walker Lane between latitudes 38°N and 39°N, extending from the Sierra Nevada near Yosemite National Park ~200 km northeast past Gabbs, Nevada. This line crosses several active normal and strike-slip faults which strike roughly north or northwest and includes the Wassuk Range and the Gumdrop and Benton Springs faults [*Wesnousky*, 2005]. The northeast end of the network passes out of the Walker Lane and penetrates into the central Basin and Range in the vicinity of the roughly north-northeast striking Fairview [*Slemmons*, 1957], Hot Springs (K. D. Adams and T. L. Sawyer, Fault number 1312, Hot Springs fault zone, in Quaternary fault and fold database, accessed June 2006, at http://earthquakes.usgs.gov/regional/qfaults), Ione Valley (T. L. Sawyer and D. J. Lidke Fault number 1334, Ione Valley Fault, in Quaternary fault and fold database of the United States, accessed June 2006, http://earthquakes.usgs.gov/regional/qfaults) fault zones, and the Gabbs Valley fault zone, which ruptured in the 1932 Cedar Mountain M7.2 earthquake [*Bell et al.*, 1999] and is shown east of the Gabbs Valley Range in Figure 2.

[27] The zone spanned by the network accommodates roughly 10 mm/yr of dextral shear between the Sierra Nevada and central Basin and Range accounting for most of the velocity signal (Figure 3e). We find that the gradient in velocity is steepest just east of the SNGV microplate, in agreement with previous results [*Oldow et al.*, 2001; *Kreemer et al.*, 2007]. Scatter in the velocities parallel to the trend of the network is ~2 mm/yr, similar to the scatter in the velocities normal to the local preferred direction in the other networks. Exceptional outliers include the continuous site DECH, and sites H130 and Z25X. On the west end of the profile, the higher values for $\chi^2$ in the strain modeling for this network (Figure 6c) indicate that the deformation field becomes more complex at the west end of the network. As for the Pyramid and Lovelock networks, this complexity may be a direct result of higher slip rates on the western-most faults or the more complex faulting patterns seen in the western part of the central Walker Lane [*Oldow*, 2003].

[28] We removed CSUN from consideration because of its proximity to the Long Valley caldera system that is known to produce local deformation signals owing to magmatic unrest [*Hill et al.*, 2003]. Because of its anomalous azimuth with respect to other velocities we also checked the effect of HNTO on strain rate estimates. However, tests indicate that because of its larger uncertainty, removing it did not have a significant impact on the inferred strain rates.

[29] The average strain rate inferred from these velocities is shear with no significant dilatation, and is very uniform in style and orientation from the west end of the network to approximately 118°W. The average strain rate for the entire zone in Figure 6a is $\varepsilon_\Delta$ = 1.8 ± 2.3 nstrain/yr, and $\varepsilon_{xy}$ = 47.8 ± 2.3 nstrain/yr. Again, we looked at two sets of subgroups, one using sites between latitudes 37.5°N and 39.5°N, and another set using sites between latitudes 37.5°N and 39°N. The second set omits most sites from the Highway 50 network to the north but uses fewer sites and hence has larger uncertainties. However, the results for the two site subset groups are very similar, indicating that the inference of deformation within the Hawthorne network is not greatly influenced by changes in the deformation field to the north. The peak shear value is ~80 nstrain/yr between longitudes 118.8°W and 119.3°W, near the California/Nevada border, west of the Wassuk fault. The shear direction is approximately N35° ± 3°W, parallel to the direction of motion of the SNGV with respect to the central Basin and Range. East of longitude 118°W, dilatation increases somewhat and coincides with a reduction in the intensity of shear strain, and can be characterized as uniaxial extension of 19.9 ± 3.0 nstrain/yr oriented N74° ± 6°W. This direction is roughly perpendicular to the average strike of the normal faults (e.g., Fairview, Paradise Range, faults). At the very northeastern end of the network, near the Ione Valley and Shoshone range, the deformation is not distinguishable from zero.

[30] Because of the close proximity of the 1932 M 7.2 Cedar Mountain earthquake it may be important to compensate for the combined effects of postseismic relaxation from this and other CNSB earthquakes. As with the Lovelock and Pyramid networks we calculated the strain rates based on corrected velocities and found that changes are significant between longitudes 118.5°W and 118°W in the northern group of Hawthorne subsets. As was the case for the Lovelock network, the strain rate values west of the CNSB faults are reduced but remain greater than zero (Table 2), indicating that either some secular deformation remains or that the relaxation model underestimates the postseismic effect. Before the correction the strain rate obtained for sites between longitudes 117.5°W and 118.5°W and latitudes 38.6°N and 39.5°N are $\varepsilon_\Delta = 33.8 \pm 12.5$ nstrain/yr, and $\varepsilon_{xy} = 55.7 \pm 12.5$ nstrain/yr but after the correction are $\varepsilon_\Delta = 21.3 \pm 12.5$ nstrain/yr, and $\varepsilon_{xy} = 32.6 \pm 12.5$ nstrain/yr (Table 2), indicating that the postseismic relaxation can explain a significant amount of both the extension and the shear deformation. Strain rate changes for the southern group of site subsets were not significant at the 95% confidence level, suggesting that the most significant transient effects came from sites north of latitude 39°N, which are more strongly influenced by upper mantle relaxation from the more recent 1954 Dixie Valley M6.8 and Fairview Peak M7.1 earthquakes [*Hetland and Hager*, 2003; *Gourmelen and Amelung*, 2005; *Hammond et al.*, 2007].

[31] The deformation field does not exhibit obvious characteristics of strain partitioning that are present in the active faulting. For example, between 118.7°W and 118.0°W dextral slip seems to occur on the Benton Springs, Gumdrop, Petrified Spring system, but the Wassuk fault, one range to the west, exhibits predominantly normal faulting [*Wesnousky*, 2005]. In fact no dilatation appears to be observed in the geodetic strain field near the Wassuk fault (Figure 6b), which is similar to the average for this entire region (Table 2). Possible explanations for this include (1) spatial smoothing of the strain rate field, causing zones of extension to be cancelled by other zones of contraction inside the same site subset, or (2) the rates of dilatation associated with area growth of this part of the Walker Lane are too small to be resolved with our current data. On the western portions of the Hawthorne profile, it may be that spatial partitioning occurs only in the upper seismogenic crust, with interseismic buried slip confined to a single oblique slip fault in the middle and lower crust.

## 4. Discussion

### 4.1. Postseismic Relaxation of the Central Nevada Seismic Belt

[32] Between the late 19th to mid-20th century at least six M > 6.5 earthquakes occurred in central Nevada. Some of these earthquakes were large enough to perturb the lithospheric stress field to upper mantle depths, and it is likely that a substantial portion of the deformation observed geodetically results from subsequent postseismic viscoelastic relaxation of the lower crust and/or upper mantle [*Savage and Church*, 1974; *Hetland and Hager*, 2003; *Gourmelen and Amelung*, 2005]. Here we have focused on the component of the Basin and Range strain rate field that results in steady state deformation of the lithosphere, most of which is likely relieved in episodic earthquakes in the upper crust. However, in order to interpret the velocity field for the Lovelock network in terms of steady state deformation, it is necessary to estimate and remove the contribution of CNSB postseismic transient deformation before calculating the strain rate field. Several studies have estimated the viscosity structure of the Basin and Range lithosphere, in various localities, using geodetic techniques to measure postseismic deformation [e.g., *Pollitz et al.*, 2000, 2001; *Nishimura and Thatcher*, 2003; *Freed and Burgmann*, 2004], or rebound following unloading of large postglacial lakes [*Nakiboglu and Lambeck*, 1983; *Bills et al.*, 1994; *Bills et al.*, 2007]. Most of these studies have concluded that the lower crust has a higher viscosity than the upper mantle (but see *Hetland and Hager* [2003] for a dissenting view). In one representative study, *Hammond et al.* [2007] predicted transient postseismic velocities from the CNSB earthquakes for the GPS sites used in the present study. Our velocities corrected for transient effects are shown in Figure 3. Subtracting the postseismic model velocities from our observed velocities and recalculating the strain rates (Figures 4b, 5b, and 6b) indicates that over 50% of the dilatation and between 25% and 50% of the shear strain between 117°W and 118.2°W can be explained by the transient deformation. This is consistent with a postseismic velocity field dominated by the effects of the Pleasant Valley normal faulting and Dixie Valley oblique normal faulting events, which produce mostly uniaxial extension in a direction normal to the strike of these faults. Near 118.5°W some dilatation still remains in the corrected velocity field, but it is not clear whether this reflects a shortcoming in the relaxation model or active extension west of the CNSB. Indeed, some extension should remain in the vicinity of the CNSB after subtracting the transient component, since secular extension of the crust is required to drive these faults to rupture and account for the long-term slip rate of ~1 mm/yr determined from paleoseismic studies of CNSB faults [*Bell et al.*, 2004].

[33] According to the *Hammond et al.* [2007] model, it does not appear that the anomalous motion of the BARGEN GPS site LEWI at Mt. Lewis, Nevada [*Wernicke et al.*, 2000], can be explained by viscoelastic relaxation of lower crust or upper mantle following the historic earthquakes of the CNSB. The model strain field has a spatial wavelength that is on the order of ~100 km or more, and thus does not produce a large variation of one GPS site velocity compared to others 10s of kilometers away. Furthermore, the site closest to LEWI, station BAMO, has been recently installed less than 30 km to the west of LEWI and shows a different behavior. The velocity of BAMO, although more uncertain owing to its shorter time series, is very similar to other nearby sites such as ELKO, MINE and TUNG (Figure 2 and Table 1). Thus it may be more likely that LEWI is affected by the large changes in groundwater levels owing to water extraction at the Cortez gold mine in Crescent Valley ~20 km southeast of LEWI [*Gourmelen and Amelung*, 2006].

### 4.2. Active Dilatation in the Western Great Basin

[34] We have shown that the western Great Basin between latitudes 38°N and 42°N is essentially a right-

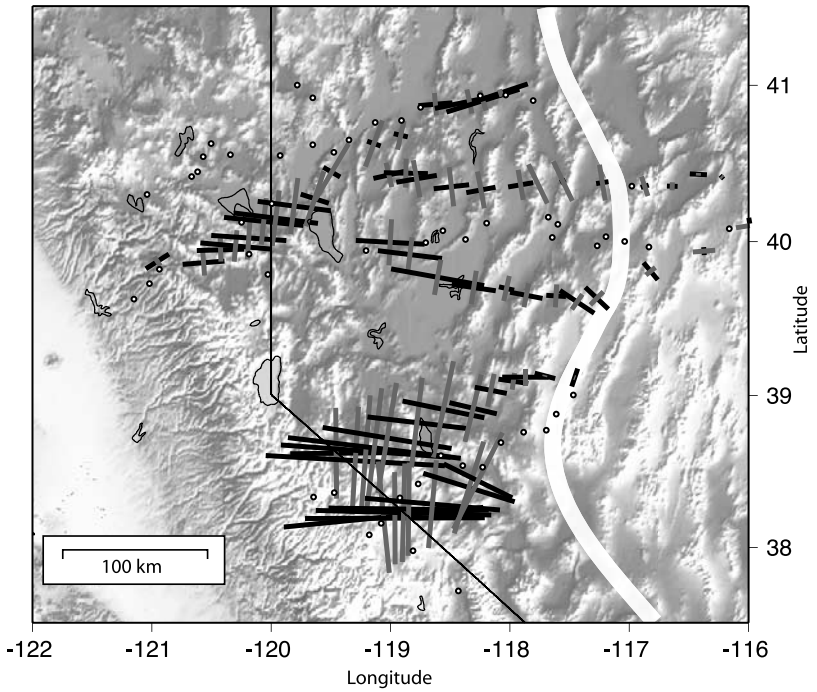


**Figure 7.** Deformation placed into regional context. White circles are the new sites presented in this study and shown in Figure 1. Horizontal strain rate tensors are represented by gray (contraction) and black (extension) crossed bars. The thick white line bounds the eastern extent of deformation that is greater than the uncertainties of our measurements. All strain rates are determined using the velocities corrected according to the postseismic relaxation model of *Hammond et al.* [2007].

lateral shear zone with a small amount of net dilatation ($\varepsilon_{xy}$ = 26.1 ± 0.8, $\varepsilon_{\Delta}$ = 2.6 ± 0.8 nstrain/yr, Table 2). The zone of deformation that is confined to the westernmost part of the Basin and Range province widens by approximately a factor of three north of latitude 39°N (compare Figures 3a to Figure 3e). We have found through trial and error sampling that the region with greatest net positive dilatation is found in the area approximately bounded by 119°W to 117°W, and 39°N to 40.5°N, although because of the averaging implicit in our strain rate estimation procedure this extension could be more spatially localized. Correcting the velocities for postseismic relaxation according to the model of *Hammond et al.* [2007] explains most, but not all, of the dilatation in this region (Figure 5b and Table 2), implying a significant amount of secular area growth northeast of the Walker Lane. However, it should be kept in mind that the *Hammond et al.* [2007] model was designed to reconcile geologic and geodetic estimates for slip rates on the CNSB faults, and hence preserve ~1 mm/yr extension across the CNSB by design.

[35] The bend in the eastern margin of the northward widening deformation zone (Figure 7) wraps around the east side of the most rapid dilatation in the Nevada Basin and Range. This correlation is consistent with the transfer of a fraction of Walker Lane dextral shear inboard to northwestward extension onto normal faults in the vicinity of the CNSB [*Faulds et al.*, 2005b]. It is also kinematically consistent with the zone of 2–3 mm/yr of east-west extension seen with GPS by *Hammond and Thatcher* [2005] in northwest Nevada, and with the transfer of deformation into the Oregon Basin and Range [*Pezzopane and Weldon*, 1993]. However, the north-northwest transfer of this extension may include two (or more) distinct zones, as is implied by the block modeling presented in the next section.

[36] Elsewhere in the central and northern WL many approximately north-south oriented normal faults exist (e.g., the Genoa, Wassuk, eastern Pyramid Lake, Bonham Ranch), consistent with the approximately E-W orientation of maximum extensional strain rate (Figure 7). The presence of these normal faults may indicate there is a small amount of dilatation near latitude 38.5°N. However, given the velocity uncertainties, such extension may be too small to be detected with a small number of sites surrounding individual faults systems. The general lack of east-west striking thrust faults suggests that the east-west extension expressed as normal faulting is not compensated by north-south shortening, and hence is an indication of net area growth of the WL. North of latitude 39°N we observe positive dilatation (Table 2), implying that the northern part of the WL is extending more rapidly.

[37] It has been proposed that some localized extension occurs as a result of misalignment of eastern boundary of the Sierra Nevada relative to the direction of SNGV block motion [*Unruh et al.*, 2003; *Oldow*, 2003; *Kreemer et al.*, 2007]. However, if the zone affected by such a releasing geometry is narrower than ~50 km, then our method of using wide aperture subsets of GPS sites determining strain rates will not be able to detect dilatation occurring within such a narrow zone. In any case, such extension is likely

**Table 3.** Model Slip Rates and Uncertainties[a]

| Fault | Strike-Slip[b] | Dip-Slip[c] | Horizontal Extension[d] | Fault Dip[e] |
|---|---|---|---|---|
| 1 | −2.5 ± 0.3 | −3.9 ± 0.4 | −2.8 ± 0.3 | −45 |
| 2 | −2.0 ± 0.3 | −2.3 ± 0.5 | −1.6 ± 0.4 | −45 |
| 3 | −2.2 ± 0.3 | −1.7 ± 0.5 | −1.2 ± 0.3 | −45 |
| 4 | 0.1 ± 0.3 | −0.6 ± 0.5 | −0.4 ± 0.4 | −45 |
| 5 | 0.4 ± 0.4 | −0.2 ± 0.5 | −0.2 ± 0.4 | −45 |
| 6 | −2.6 ± 0.2 | 0.6 ± 1.0 | 0.1 ± 0.2 | −80 |
| 7 | −2.6 ± 0.2 | −0.8 ± 1.0 | −0.1 ± 0.2 | −80 |
| 8 | −2.6 ± 0.2 | −2.2 ± 1.2 | −0.4 ± 0.2 | −80 |
| 9 | −2.5 ± 0.2 | −3.0 ± 1.5 | −0.5 ± 0.3 | −80 |
| 10 | −1.2 ± 0.4 | −3.1 ± 0.6 | −2.2 ± 0.4 | −45 |
| 11 | −2.5 ± 0.4 | 7.4 ± 2.1 | 1.3 ± 0.4 | −80 |
| 12 | −2.7 ± 0.2 | −1.1 ± 1.3 | −0.2 ± 0.2 | −80 |
| 13 | −2.7 ± 0.2 | −0.6 ± 1.2 | −0.1 ± 0.2 | −80 |
| 14 | −2.6 ± 0.2 | −2.3 ± 1.2 | −0.4 ± 0.2 | −80 |
| 15 | −2.5 ± 0.2 | −4.9 ± 1.3 | −0.9 ± 0.2 | −80 |
| 16 | −2.2 ± 0.2 | −7.4 ± 1.5 | −1.3 ± 0.3 | −80 |
| 17 | −1.9 ± 0.3 | −1.0 ± 0.4 | −0.7 ± 0.3 | 45 |
| 18 | −1.6 ± 0.3 | −1.7 ± 0.4 | −1.2 ± 0.3 | 45 |
| 19 | −1.4 ± 0.3 | −2.0 ± 0.3 | −1.4 ± 0.2 | −45 |
| 20 | −1.8 ± 0.3 | −1.5 ± 0.3 | −1.0 ± 0.2 | −45 |
| 21 | −1.8 ± 0.3 | −1.3 ± 0.3 | −1.0 ± 0.2 | −45 |
| 22 | −1.4 ± 0.3 | −2.2 ± 0.4 | −1.6 ± 0.3 | −45 |
| 23 | −0.7 ± 0.3 | −1.5 ± 0.5 | −1.1 ± 0.3 | −45 |
| 24 | −1.2 ± 0.3 | −0.9 ± 0.5 | −0.6 ± 0.3 | −45 |
| 25 | −0.8 ± 0.3 | −1.6 ± 0.5 | −1.1 ± 0.3 | −45 |
| 26 | −1.2 ± 0.3 | −1.0 ± 0.5 | −0.7 ± 0.3 | −45 |
| 27 | −3.5 ± 0.2 | 0.5 ± 0.3 | 0.3 ± 0.2 | −45 |
| 28 | −3.2 ± 0.2 | −8.5 ± 1.1 | −1.5 ± 0.2 | −80 |
| 29 | −3.6 ± 0.2 | 0.5 ± 0.9 | 0.1 ± 0.2 | −80 |
| 30 | −0.0 ± 0.2 | 0.4 ± 0.3 | 0.3 ± 0.2 | −45 |
| 31 | −0.1 ± 0.2 | 0.3 ± 0.3 | 0.2 ± 0.2 | −45 |
| 32 | −0.0 ± 0.2 | 0.3 ± 0.3 | 0.2 ± 0.2 | −45 |
| 33 | −0.1 ± 0.2 | 0.3 ± 0.3 | 0.2 ± 0.2 | 45 |
| 34 | −0.1 ± 0.2 | 0.2 ± 0.3 | 0.1 ± 0.2 | 45 |
| 35 | −0.1 ± 0.2 | 0.1 ± 0.4 | 0.1 ± 0.3 | 45 |
| 36 | 1.1 ± 0.4 | 2.2 ± 1.8 | 0.4 ± 0.3 | −80 |
| 37 | 1.6 ± 0.2 | −3.5 ± 1.4 | −0.6 ± 0.2 | −80 |
| 38 | −0.3 ± 0.2 | 0.1 ± 1.2 | 0.0 ± 0.2 | −80 |
| 39 | −0.5 ± 0.2 | 0.2 ± 0.2 | 0.2 ± 0.2 | 45 |
| 40 | −0.4 ± 0.1 | −0.5 ± 0.2 | −0.4 ± 0.2 | 45 |
| 41 | −0.4 ± 0.1 | −0.7 ± 0.2 | −0.5 ± 0.1 | −45 |
| 42 | −0.2 ± 0.1 | −1.1 ± 0.2 | −0.7 ± 0.1 | −45 |
| 43 | −0.2 ± 0.1 | −1.3 ± 0.2 | −0.9 ± 0.2 | 45 |
| 44 | −0.8 ± 0.2 | −0.9 ± 0.2 | −0.6 ± 0.2 | 45 |
| 45 | −0.6 ± 0.2 | −1.3 ± 0.3 | −0.9 ± 0.2 | 45 |
| 46 | −0.5 ± 0.2 | −1.7 ± 0.4 | −1.2 ± 0.3 | 45 |

[a]Slip rates are in mm/yr.
[b]Left-lateral slip rate is positive, right-lateral negative.
[c]Thrust slip rate is positive, normal slip rate is negative.
[d]Horizontal extension is dip-slip rate times cos(dip).
[e]Dips in degrees, positive (negative) dip is down to left (right).

confined near the SNGV and cannot explain the pervasive normal faulting that has been active in the province for 10–15 million years and still may be active today [*Wesnousky et al.*, 2005; U.S. Geological Survey and Nevada Bureau of Mines and Geology, Quaternary fault and fold database for the United States, accessed June 2006, http://earthquakes.usgs.gov/regional/qfaults].

### 4.3. Block Modeling of the Northern Walker Lane

[38] In order to better characterize the along strike variations in strain accumulation patterns, we estimate the total rate of motion across several transects spanning the WL at various latitudes. This provides constraints on the integrated slip on faults across these zones, and serves as a basis for comparison to geologic estimates of slip rates in the region. To this end, we have implemented a block modeling strategy (Appendix A) that divides the region into contiguous blocks bounded by faults. Each block is a spherical cap whose motion is parameterized with three values in a rotation vector that is constrained by all of the GPS velocities on the block. Perturbations to rigid body rotation occur around the block boundaries to account for interseismic strain accumulation on block bounding faults. This implementation ensures kinematic consistency in the sense that (1) fault slip rate and style are a direct consequence of relative block motion, (2) elastic strain accumulation is taken into account where blocks in contact are locked at the surface during the observation period, and (3) slip is continuous along boundaries and accordingly changes style with changing fault orientation and interblock relative motion. Our modeling is similar in strategy to recent block modeling studies of the western United States [e.g., *McClusky et al.*, 2001; *Miller et al.*, 2001; *McCaffrey*, 2002; *d'Alessio et al.*, 2005; *McCaffrey*, 2005; *Meade and Hager*, 2005] but is focused in our region where kinematic constraints have been poor until now. Also, in our model no faults are allowed to creep in the seismogenic upper crust, since we are not aware of any evidence for surface creep on normal faults in the Basin and Range. All deformation of the blocks is elastic, i.e., no permanent deformation of the blocks is allowed. We use this modeling to explore the relationship between our measured GPS velocities and the slip rates and sense of motion on the active faults of the region.

[39] We have designed the block model using identified active faults found in the USGS Quaternary Fault and Fold database (U.S. Geological Survey and Nevada Bureau of Mines and Geology, Quaternary fault and fold database for the United States, accessed June 2006, http://earthquakes.usgs.gov/regional/qfaults). In some cases we introduced model faults that bridge gaps between known faults in order to complete block boundaries and ensure kinematic consistency. Because of the large number of faults in the western Basin and Range, and because of the relatively immature state of knowledge (e.g., compared to southern California) about which of the faults accommodate the most slip, the block-building process necessarily contains some elements of subjective choice. In these cases the presence of topographic lineaments, older faults, the orientation of the strain rate field, or earthquake locations were used to make judgments about where block boundaries should reside. Normal faults were assumed to dip 45° toward their headwalls in accordance with the global average dip for normal faults [*Thatcher and Hill*, 1991]. Strike-slip faults were assigned a dip of 80° in order to allow for the possibility of some extension (Table 3). All locking depths were assigned to be 15 km depth, in general agreement with the maximum depth of most Basin and Range seismicity, and with the maximum allowed depth inferred for coseismic ruptures at the CNSB (14 km) [*Hodgkinson et al.*, 1996]. Our model has sufficient complexity to constrain the integrated slip style and rate across the four transects through our study area shown in Figures 8a and 8b and suggest possible partitioning of slip within the broadly defined deforming zones. The velocities predicted by our model and residual velocities (GPS velocities minus the velocities predicted by the model) are shown in Figure 9.

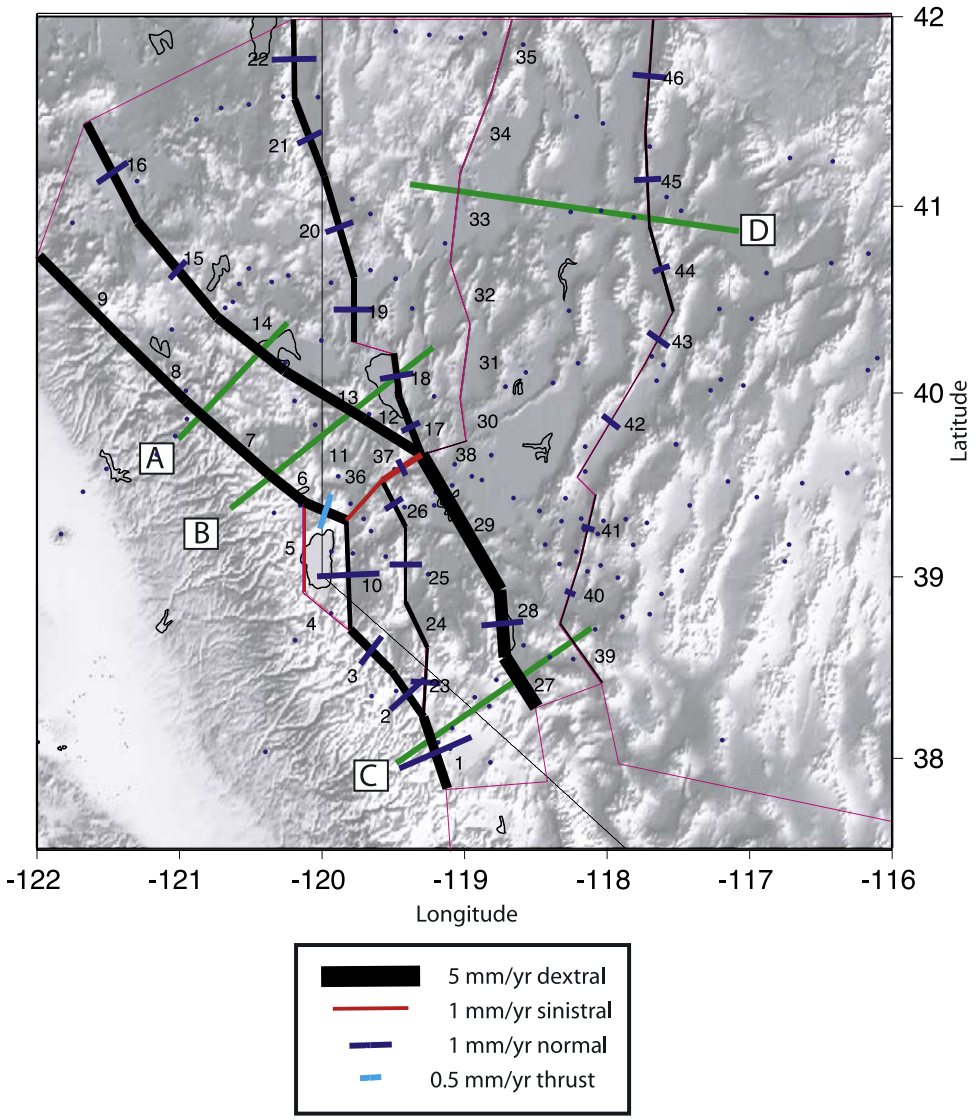


**Figure 8a.** Block model of northern Walker Lane and adjoining areas including CNSB. Thickness of black (red) line segments indicate the dextral (sinistral) component of inferred slip rate. Length of blue (cyan) fault segment bisecting bar indicates the normal (thrust) component of slip. Thin magenta lines indicate block boundaries for which no slip rate was inferred. Blue dots are locations of the GPS velocities used to constrain the model. Green line segments are deformation zone transects discussed in section 4.3.

[40] For our block model the overall misfit $\chi^2 = 3.3$ is defined the same as in (2) except that the number of free parameters is three times the number of blocks. Because most sites are not near (within 20 km of) block boundaries, this misfit is not very sensitive to small changes in the predefined geometry of the blocks or the dip of faults. Change in the assumed strike of block boundaries, however, can alter the inferred partitioning between strike-slip and extensional slip on any given fault segment, but do not strongly affect the overall secular motion of the blocks. Thus comparisons between the sense of slip obtained in our modeling and sense of slip geologically, or seismically, observed at specific localities should be made with the resolution of our fault model borne in mind. The overall misfit of our model to the data suggests that there is significant amount of signal in the GPS data that is not accounted for in our model. In Section 2.2, we opted not to increase our uncertainties in order to scale the misfit to 1 for a constant strain rate model, however, that scaling factor (1.34) would not have been large enough to reduce the overall block model misfit to unity. It would have been nearly sufficient to do so, however, for the best fitting blocks in our model (Surprise and EBR, Table 4), which are the slowest deforming areas in the model, suggesting that where the WL is deforming most rapidly our model may not be sufficiently complex to account for all the details of crustal deformation.

[41] The slip rates for each block bounding fault segment are shown in Figure 8a and listed in Table 3. The block

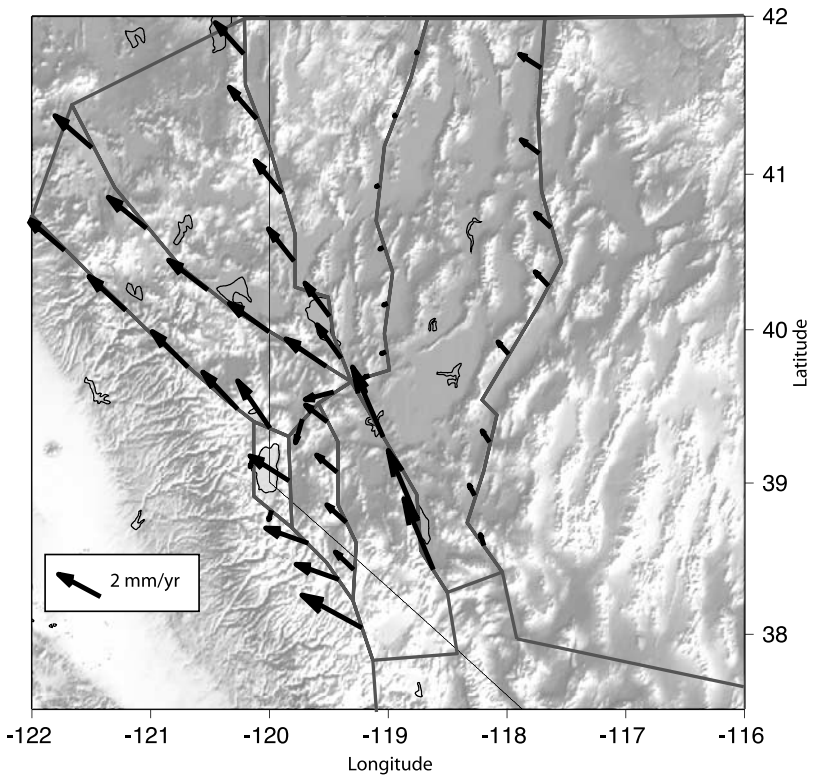


**Figure 8b.** Relative velocities between adjacent blocks for model shown in Figure 8a. Velocity vectors shows rate of motion of more western block with respect to the adjacent block to the east.

rotation Euler pole locations and rates are found in Table 5. The sense and rate of relative motion across faults that bound adjacent blocks is illustrated in Figure 8b. The first-order properties of the model can be seen in the sum of model slip rates along four transects that we have defined across the central to northern Walker Lane (Figure 8a). We discuss each of these transects individually below.

[42] Transect A crosses the Mohawk Valley (model fault segment 7) and Honey Lake faults (model fault segment 14) where the model slip rates are dextral 2.3 ± 0.3 and 2.1 ± 0.3 mm/yr, respectively, with extensional rates that are not significantly different from zero (Table 3). The relatively large misfit for the Mohawk Block (Table 4) is driven by the site SLID, which is a continuous GPS site with relatively low uncertainties, and possibly anomalous motion associated with magmatic activity [*Smith et al.*, 2004]. This site alone would suggest greater counterclockwise rotation than is permitted by other GPS velocities on the block. Running the model without the site SLID, however, does not significantly change the estimates for slip rates on the Mohawk Valley or PHL fault systems. New GPS sites within the Mohawk block would result in better constraints on the location of its rotation axis and rate of rotation.

[43] Transect B crosses the same faults ~50 km to the southeast, and also crosses the east Pyramid Lake fault where the three dextral slip rates are, from southwest to northeast, 2.3 ± 0.3, 2.1 ± 0.3, and 1.0 ± 0.3 mm/yr, respectively. In this transect, only the east Pyramid Lake fault, which is a prominent range front normal fault, has a significant extensional rate of 0.9 ± 0.4 mm/yr (the dip-slip rate has been projected to the horizontal). The vector sum of slip rates across this transect is ~6 mm/yr, and thus together accommodate most of the deformation across the western Basin and Range at this latitude. This is near the lower end of the range of 6–8 mm/yr estimated by *Dixon et al.* [2000] for the sum of slip rates across the Mohawk Valley and Honey Lake fault systems. It is also consistent with the 6–8 mm/yr of velocity gradient occurring west of the CNSB observed by *Thatcher et al.* [1999]. On the nearby Olinghouse fault we infer significant left-lateral slip (e.g., segment 36 has 2.0 ± 0.4 mm/yr), which is a consequence of the rotation of the blocks to the south and north. This is consistent with the style of slip inferred from geological investigation of the fault [*Briggs and Wesnousky*, 2005].

[44] Transect C crosses three model faults spanning the central Walker Lane from the SNGV block to the Toiyabe Range east of Gabbs, Nevada. At the Sierra Nevada range front (segment 1) we infer dextral and extensional slip rates of 2.1 ± 0.3 and 1.3 ± 0.4 mm/yr, respectively. Farther east, at the southern end of the Wassuk fault we infer 3.0 ± 0.3 mm/yr dextral slip, and no extension. However, significant extension of 1.5 ± 0.3 mm/yr occurs on its more north-south striking segment near Walker Lake, illustrating the sensitivity of the sense of slip on the model fault strike. At the northeast end of the transect, near the Gabbs Valley Range and the Benton Springs/Petrified Springs faults, the inferred dextral rate is 0.4 ± 0.2 with 0.2 ± 0.2 extension. The sum of slip rates across this transect is low (magnitude of vector sum is 5.9 mm/yr) compared to the velocity change across this part of the Walker Lane (Figures 3e

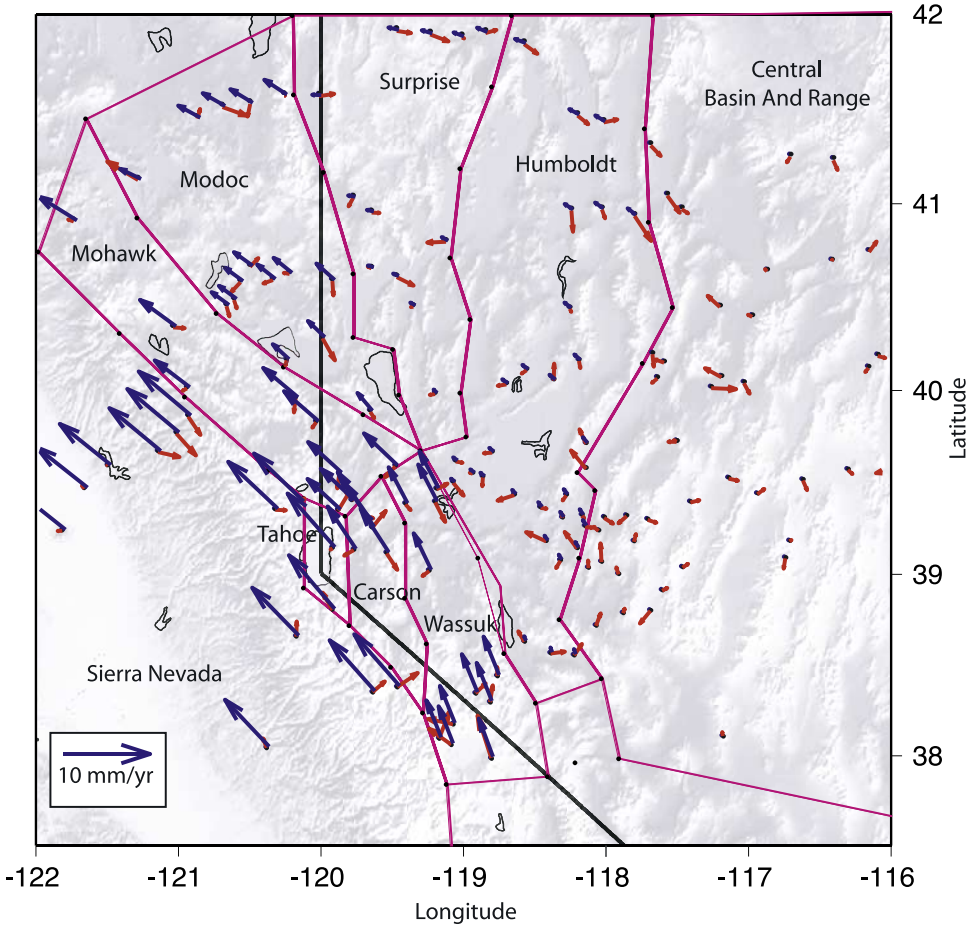


**Figure 9.** Residual velocities (red) consisting of the GPS velocities minus the velocities inferred from the block model. Model velocities across the Walker Lane (blue) are shown with respect to the central Basin and Range (from Table 5) from the predicted velocities. Blocks are labeled with names used in Table 5.

and 3f). This is due in part to a systematic misfit between model and data at the level of ~2 mm/yr in the N35°W component of velocity between Gabbs Valley Range and continuous GPS site GABB at the east end of the Hawthorne network (Figure 3e). There is also substantial misfit near the west end of this network, where scatter in the N35°E component of velocity is large, but the model closely matches the velocities of the continuous stations DYER and DECH. Together these misfits suggest that there may be significantly more deformation occurring near the east end of the Hawthorne network than is permitted by our block model. Also, the Wassuk block may need to be further divided to allow for relative motion between its southern and northern halves.

[45] The largest strike-slip rate in the model occurs across fault segments 27–29, which are the Wassuk fault and its northern extent into the Churchill Valley southwest of the Carson Sink. This high rate was unexpected since the trace of a major throughgoing strike-slip fault is not well mapped here, nor is it likely to be as linear as is indicated in our simple model. We speculate that the strike-slip motion in our model is representative of a more complex pattern of transfer of ~3 mm/yr right-lateral relative motion across this zone. The presence of a major boundary in this area is in agreement with the analysis of *Oldow* [2003], who suggested on the basis of GPS measurements and seismicity patterns that this area marks a transition between wrench-dominated and extension-dominated behaviors. On the basis of Figure 8a and Table 3 we do detect a fundamental difference in character of the deformation on either side of this boundary. The faults to the east of this boundary are inferred to have almost completely normal slip, while faults

**Table 4.** Misfits for Each Block

| Block | $\chi_2$ per DOF[a] |
|---|---|
| SNGV | 5.0 |
| Mohawk | 8.1 |
| Modoc | 3.6 |
| Surprise | 3.1 |
| Humbolt | 4.1 |
| EBR | 3.1 |
| Tahoe | 30.2 |
| Carson | 5.9 |
| Wassuk | 9.0 |

[a]See equation (2) for definition. Note that in this case the degrees of freedom (DOF) is 2 times the number of sites on the block minus 3 free parameters.

**Table 5.** Euler Pole Rotation Rates of Model Blocks With Respect to SNARF-NA[a]

| Block | Pole Latitude | Pole Longitude | Rotation Rate | Correlation | N |
|---|---|---|---|---|---|
| SNGV | −55.0 ± 10.8 | 166.8 ± 24.8 | 0.117 ± 0.025 | −0.160 | 14 |
| Mohawk | −61.7 ± 12.2 | 104.6 ± 16.2 | 0.149 ± 0.031 | −0.237 | 14 |
| Modoc | −58.2 ± 21.3 | 150.4 ± 46.2 | 0.073 ± 0.031 | −0.328 | 14 |
| Surprise | −57.1 ± 17.9 | 86.4 ± 18.6 | 0.108 ± 0.034 | 0.063 | 16 |
| Humbolt | −53.9 ± 11.4 | 77.4 ± 11.4 | 0.147 ± 0.029 | 0.219 | 22 |
| EBR | −45.8 ± 3.7 | 66.9 ± 3.5 | 0.309 ± 0.020 | 0.337 | 14 |
| Tahoe | −38.8 ± 16.4 | −173.0 ± 25.8 | 0.109 ± 0.029 | 0.062 | 5 |
| Carson | −39.0 ± 20.3 | −178.3 ± 32.2 | 0.088 ± 0.028 | 0.015 | 9 |
| Wassuk | −57.2 ± 15.2 | 107.3 ± 18.0 | 0.132 ± 0.034 | −0.279 | 12 |

[a]Rotation rate is in degrees per million years. Latitude/longitude are in degrees. Uncertainties are one standard deviation. N is number of GPS sites on block. Correlation is correlation between pole latitude and longitude.

to the west exhibit significant components of both normal and dextral slip, i.e., are transtensional.

[46] Transect D crosses the CNSB near latitude 41°N, just north of the Tobin Range and the surface rupture from the 1915 Pleasant Valley earthquake. It crosses two model fault segments, the eastern fault representing a northern extension of the CNSB (segment 45) for which we infer an extension rate of 0.6 ± 0.3 mm/yr and a strike-slip rate not significantly different from zero. This is the region where *Hammond and Thatcher* [2005] inferred a zone of ~2–

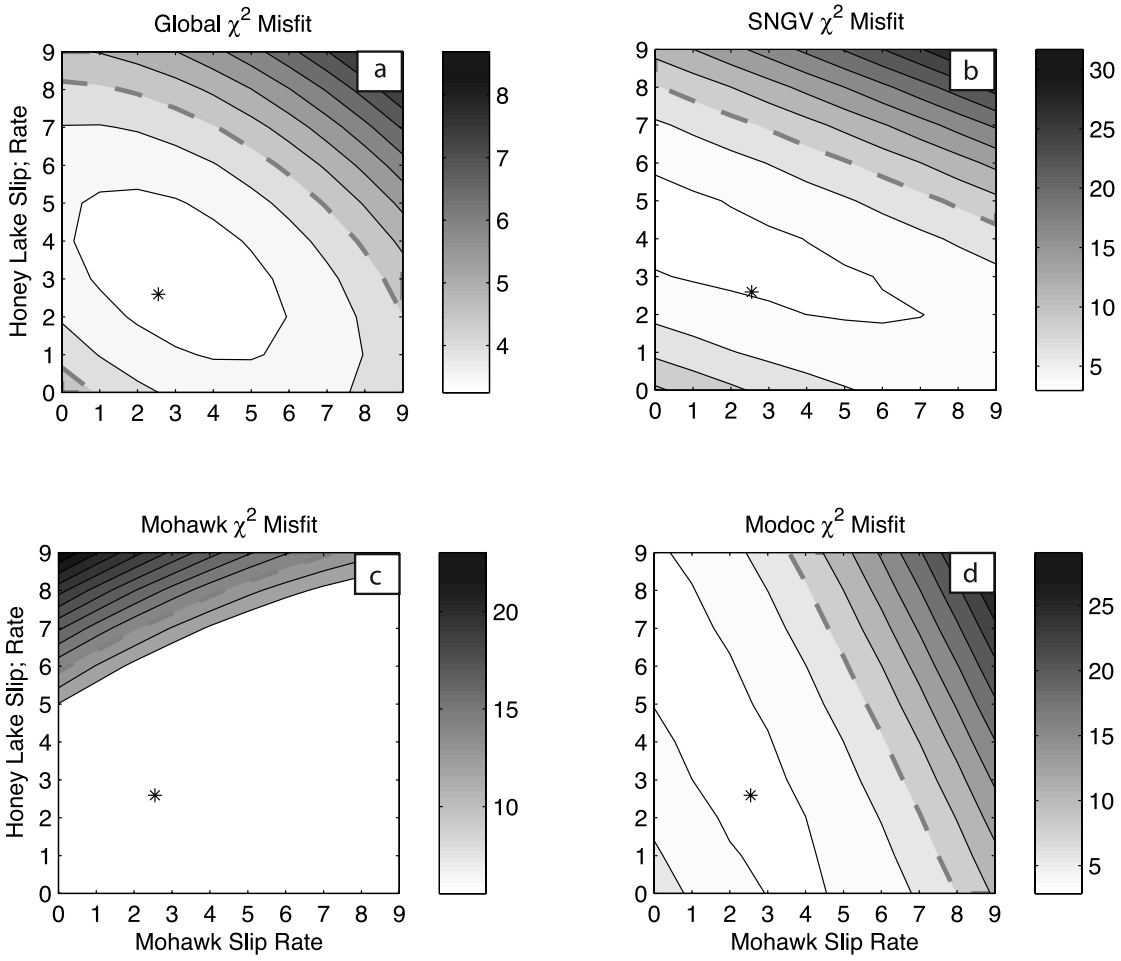


**Figure 10.** (a) Contour of misfit between model and data for selected assumed slip rates (in mm/yr) on the Mohawk Valley and Warm Springs/Honey Lake fault system. Star represents the values obtained in the preferred model presented in Figures 8a and 8b. The third contour from the minimum $\chi^2$ value (indicated with thick gray dashed contour) indicates the threshold above which models are significantly worse than the best model to 95% confidence. (b, c, and d) Same as Figure 10a for subsets of sites on the SNGV, Mohawk, and Modoc blocks, respectively.

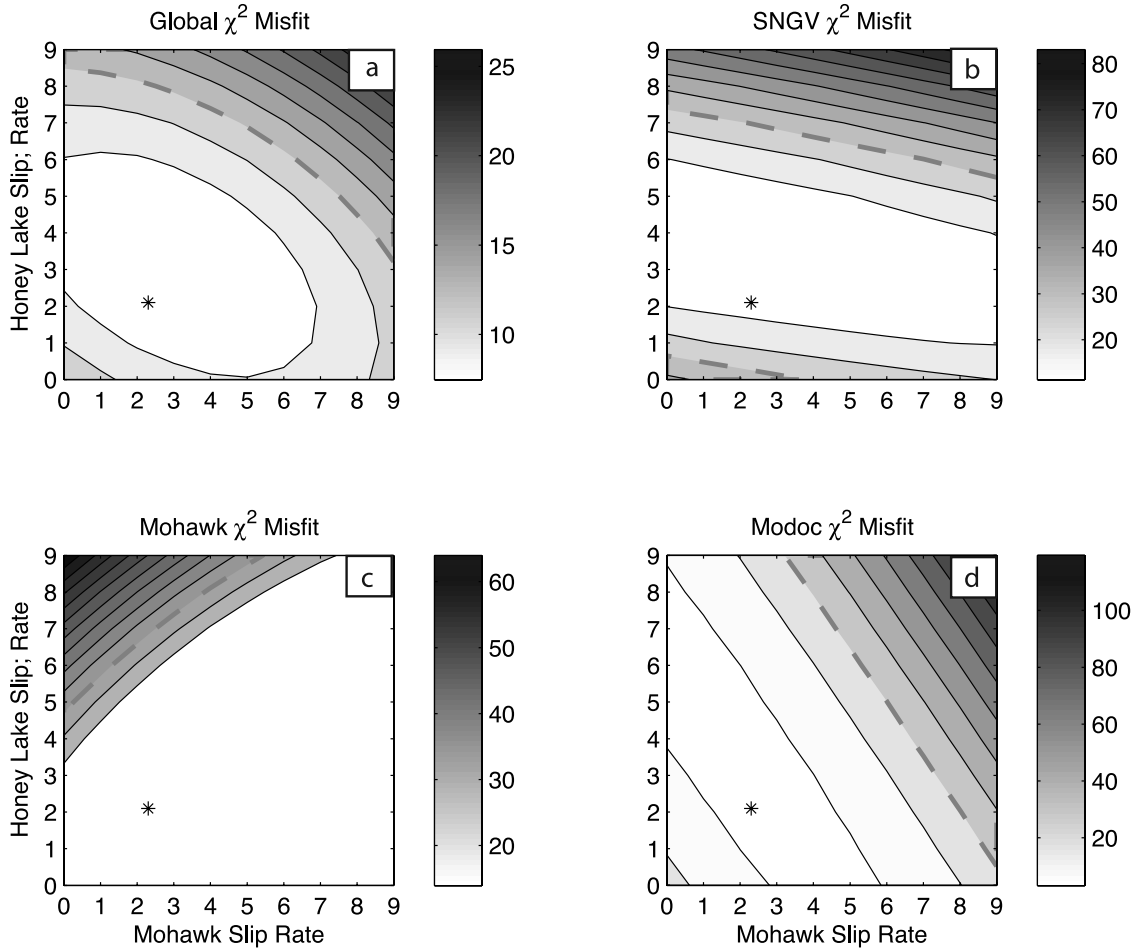


**Figure 11.** Same as Figure 10, except that all continuous GPS sites have been assigned velocity uncertainties of 0.1 mm/yr in the forward modeling and misfit estimation. Slip rates are in mm/yr.

3 mm/yr east west extension from velocities uncorrected for postseismic relaxation. It is likely that at least part of the extension inferred from *Hammond and Thatcher* [2005] was attributable to postseismic relaxation, with the rest of it accommodated farther west. Here we model (using velocities adjusted for postseismic relaxation) this remaining deformation as localized on the Surprise Valley fault, where extension is 1.2 ± 0.4 mm/yr. To the west this transect crosses the Black Rock fault system where neither strike-slip nor extension rates are significantly different from zero. The extension rate is small but significant (<0.5 mm/yr) at some places on the boundary between the Humboldt and Modoc blocks, but the sinistral slip rate, is nowhere significant. The extension rate on the northwest Nevada faults diminishes northward and is statistically indistinguishable from zero at the Oregon border, as previously inferred from GPS measurements by *Hammond and Thatcher* [2005]. Although Holocene and late Quaternary offsets indicate active normal faulting on the Alvord-Steens fault zone in southeast Oregon [*Hemphill-Haley et al.*, 1999, 2000; S. F. Personius, Fault number 856c, Steens fault zone, Alvord section, accessed June 2006, http://earthquakes.usgs.gov/regional/qfaults/], extension rates appear to be below the resolution of our current GPS data.

### 4.4. Trade-offs and Sensitivity in Slip Rates

[47] Trade-offs in slip rates between adjacent fault systems can be quantified by determining the misfit to models derived subject to a priori constraints on the slip rates. For the Mohawk Valley faults system (fault segments 7 and 8) and the Honey Lake/Warm Springs system (fault segments 13 and 14) we assumed various slip rate values in order to estimate how much they can change before the data are violated to a significant degree. Significance is determined by applying an $F$ test that finds the threshold $\chi^2$ value above which the test model has 95% or greater chance to be different than our preferred model. For each test model we choose a dextral strike-slip rate for each fault system and then recalculate the global set of block rotations and other slip rates so that every model evaluated is internally self-consistent. The misfits of these test models show that the global data misfit is not significantly violated until changes in slip rate of several millimeters per year are imposed on the Mohawk Valley and Honey Lake/Warm Springs systems (Figure 10a). Thus the global misfit is relatively insensitive to these individual slip rates, and by this criterion alone the slip rates on these faults could be significantly higher. This is attributable in part to the scarcity of GPS sites on the Mohawk Block, and also to

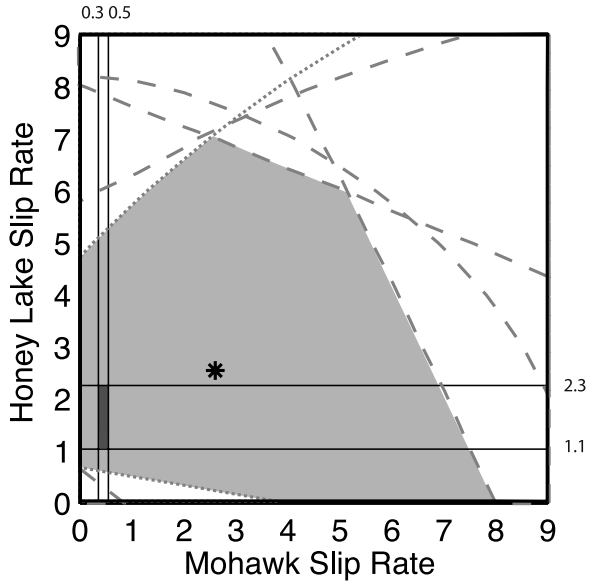


**Figure 12.** Overlap of areas inside dashed contours shown in Figures 10 and 11. Gray area is region that does not violate regional and local GPS constraints on fault slip rates (in mm/yr). Horizontal (vertical) bars show limits of slip rates estimated paleoseismically for the Honey Lake (Mohawk Valley) fault systems (see text for discussion). Dark gray area shows region where geodetic and geologic data are satisfied. Dashed lines are limits from Figure 10, and dotted lines are from Figure 11.

the proximity of the site QUIN to the Mohawk valley fault, which makes it insensitive to the slip rate on this fault. Evaluating the misfits of the SNGV, Mohawk and Modoc blocks individually (Figures 10b–10d) shows that requiring data on each of these blocks to fit the data individually can somewhat reduce the range of allowable slip rates. Additionally, we have tested the sensitivity of the modeling of slip rates to the assignment of uncertainties to the continuous GPS sites in our region. Since we have used uncertainties that are relatively large (~0.4 mm/yr on average) compared to the formal uncertainties claimed by some authors (e.g., 0.1–0.2 mm/yr [*Davis et al.*, 2003] and 0.05–0.8 [*Bennett et al.*, 2003], although the smallest of these were acknowledged by Bennett et al. to be likely too small), we have tested the effect of using uncertainty of 0.1 mm/yr. The result shows that there is a small reduction in the size of the region that can be fit by the data (Figure 11a), and that the slip rates are more sensitive to the GPS data on the nearby blocks (Figures 11b–11d). More precise continuous velocities are especially effective at eliminating the possibility that slip rates on the Honey Lake/Warm Springs system are below ~1 mm/yr (Figure 11b). Scaling the velocity uncertainties has only this small effect on the size of the region of allowable slip rates because the size of the region is controlled by model misfit rather than formal uncertainty in model parameters. If we assume that nearby GPS constraints must be satisfied as well as all the data inside our study area, then the overlap of areas inside the dotted contours in Figures 10 and 11 is the region of allowable slip rates (Figure 12).

[48] Some extreme model slip rates may not directly violate the data to 95% confidence (e.g., 7 mm/yr for Mohawk Valley and 2 mm/yr for Honey Lake) but may imply unexpected rates and styles of slip on other faults in their vicinity (e.g., thrust on demonstrably normal faults). This suggests that introducing geologic constraints on the style of slip on faults will have a significant impact on the uncertainty of the modeled slip rates. For example, geologic investigation of the Mohawk Valley fault zone has yielded a slip rate of 0.3–0.5 mm/yr of dextral slip motion [*Sawyer et al.*, 2005], and investigation of the Honey Lake fault has yielded an estimate of 1.1 to 2.3 mm/yr [*Wills and Borchardt*, 1993]. Assuming that both of these estimates are correct does not violate the geodetic data (Figure 12). Furthermore, using these rates as kinematic constraints in the block modeling does not produce any significant inconsistencies between predicted and observed slip sense on other faults in the model. Thus this pair of slip rates is a viable alternative to the best fitting model presented in Figure 8a. Constraining all of the faults in the northern WL with geologically estimated rates will greatly improve overall constraints of block motion, and will be the topic of a future study.

## 5. Conclusions

[49] We have presented geodetic velocities for 252 points with respect to stable North America, measured with GPS. The strain rates inferred from these velocities are consistent with the western Great Basin, including the central and northern WL, behaving essentially as a shear zone with minor but significant dilatation. North of latitude 39°N the shear zone is wider by approximately a factor of three. Most of the 11 mm/yr of relative motion that occurs across the central Walker Lane, near latitude 38°N, continues northwestward as dextral shear through the northern Walker Lane near latitude 40°N. The remaining deformation continues northward in a 100–150 km wide zone that deforms by a combination of dextral shear and uniaxial extension. In the vicinity of the CNSB a correction made using a model of postseismic viscoelastic relaxation associated with historic CNSB earthquakes reduces the inferred dilatation. However, significant shear and dilatation remain within the north trending zone of deformation lying to the east that includes the CNSB. Block modeling of the Walker Lane suggests that most of the western Basin and Range deformation between 40°N and 41°N latitude occurs as dextral shear across the Mohawk Valley and Pyramid/Warm Springs/Honey Lake faults systems, with lesser amounts of extension and shear occurring farther east.

## Appendix A: Block Modeling Strategy

[50] We assume that the surface motion can be approximated as piecewise continuous block rotations on a sphere, and that at the boundaries of the blocks are in contact, locked at the surface but slipping continuously at depth [e.g., *Savage and Burford*, 1973]. Since our strategy for extending the concept to many blocks bounded by finite fault segments is similar to those of other recently introduced block modeling schemes [e.g., *Bennett et al.*, 1996; *Prawirodirdjo et al.*, 1997; *Souter*, 1998; *McClusky et al.*,

2001; *Murray and Segall*, 2001; *McCaffrey*, 2002, 2005; *Meade and Hager*, 2005], we express our formulation briefly. We further assume that the GPS velocities represent the interseismic velocity field, i.e., they have been measured between large earthquakes and the effects of nonsecular processes are either nonexistent or have been estimated and removed. Thus the long-term velocity (averaged over many seismic cycles) is equal to the sum of the interseismic and coseismic velocity

$$\vec{v}_{LT} = \vec{v}_{Int} + \vec{v}_{Cos} \tag{A1}$$

or equivalently,

$$\vec{v}_{Int} = \vec{v}_{LT} - \vec{v}_{Cos} \tag{A2}$$

[51] This implements the "back-slip" approach introduced by *Savage* [1983]. In this context "coseismic velocity" is defined as the rate of movement of a point near the fault associated with coseismic offsets averaged over many seismic cycles.

[52] For GPS velocity vector $i$ with position $r_i$ on block $j$

$$\vec{v}_{GPS,i} = \vec{\omega}_j \times \vec{r}_i - \left(a_k \vec{G}_{ss,k} + b_k \vec{G}_{N,k}\right) \tag{A3}$$

where $\vec{\omega}_j$ is an unknown block rotation vector. The slip rates $a_k$ and $b_k$ are unknowns that scale the Greens functions $G_{SS}$ and $G_N$ representing the pattern of strike-slip and normal slip, respectively, for each fault segment $k$. These Green's functions are calculated for each fault segment using the functions of *Okada* [1985, 1992], since the dip, length, width and depth of the fault are predefined and unit slip is assumed to be sinistral for $G_{SS}$ and updip for $G_N$. Since GPS sites can be affected by elastic strain accumulation on more than one fault segment, especially in complex zones with densely spaced faults, we modify (A3) to include the effects of multiple nearby fault segments

$$\vec{v}_{GPS,i} = \vec{\omega}_j \times \vec{r}_i - \sum_{k=1}^{L} \left(a_k \vec{G}_{ss,k} + b_k \vec{G}_{N,k}\right) \tag{A4}$$

where $L$ is the number of nearest fault segments included. Since our data comprise only horizontal components of velocity, we need to project the model into the horizontal plane before writing out the matrix equation

$$\vec{v}_{N,i} = \left[\vec{\omega}_j \times \vec{r}_i - \sum_{k=1}^{L} \left(a_k \vec{G}_{ss,k} + b_k \vec{G}_{N,k}\right)\right] \bullet \vec{e}_{N,i} \tag{A5}$$

$$\vec{v}_{E,i} = \left[\vec{\omega}_j \times \vec{r}_i - \sum_{k=1}^{L} \left(a_k \vec{G}_{ss,k} + b_k \vec{G}_{N,k}\right)\right] \bullet \vec{e}_{E,i} \tag{A6}$$

where $\vec{e}_{N,i}$ and $\vec{e}_{E,i}$ are the unit basis vectors at site $i$ in the north and east directions, respectively.

[53] However, the slip rates on faults ($a_k$ and $b_k$) are completely determined by the relative motion of the blocks and the predefined block geometries and fault dips. Thus, effectively, the only parameters that need to be free are the block rotations ($\omega_j$). To enforce this, we write an additional constraint that the relative motion of the blocks should be related to the slip rate at the fault

$$\vec{\omega}_{j_1} \times \vec{p}_k - \vec{\omega}_{j_2} \times \vec{p}_k = a_k \delta\vec{G}_{SS,k} + b_k \delta\vec{G}_{N,k} \tag{A7}$$

where $\delta\vec{G}_{SS,k}$ and $\delta\vec{G}_{N,k}$ are the full strike-slip and dip-slip motion vector slip rates, respectively, in the global reference frame across fault $k$ defined as

$$\delta\vec{G}_{SS,k} = \vec{G}_{SS}(\vec{p}_k + \vec{\varepsilon}) - \vec{G}_{SS}(\vec{p}_k - \vec{\varepsilon}) \tag{A8}$$

$$\delta\vec{G}_{N,k} = \vec{G}_{N}(\vec{p}_k + \vec{\varepsilon}) - \vec{G}_{N}(\vec{p}_k - \vec{\varepsilon}) \tag{A9}$$

where $\vec{\varepsilon}$ is a small vector that points in a horizontal direction normal to the fault segment, and $\vec{p}_k$ is the midpoint of fault segment $k$. This constraint (A7) is equivalent to assuming that the horizontal long-term rate of relative motion across block boundaries is equal to the horizontal projection of the slip rate on the fault. The distinction is important because it is the basis for forcing the slip rate on the fault to be determined by all data on the block, not just data near the fault. Adding these constraints results in $2N + 2P$ equations that constrain $3M + 2P$ unknowns, where $N$ is the number of GPS velocities, $P$ the number of fault segments and $M$ the number of blocks.

[54] We are helped by the identity

$$\vec{u} \bullet (\vec{v} \times \vec{w}) = -\vec{v} \bullet (\vec{u} \times \vec{w}) \tag{A10}$$

because we can rearrange (A5)–(A7) so that the Euler rotation vector becomes the dotted vector, which is convenient for building a matrix equation to solve for the rotation vectors using the horizontal velocities as data. These equations become

$$v_{N,i} = -\vec{\omega}_j \bullet \left(\vec{e}_{N,i} \times \vec{r}_i\right) - \left[\sum_{k=1}^{L} \left(a_k \vec{G}_{ss,k} + b_k \vec{G}_{N,k}\right)\right] \bullet \vec{e}_{N,i} \tag{A11}$$

$$v_{E,i} = -\vec{\omega}_j \bullet \left(\vec{e}_{E,i} \times \vec{r}_i\right) - \left[\sum_{k=1}^{L} \left(a_k \vec{G}_{ss,k} + b_k \vec{G}_{N,k}\right)\right] \bullet \vec{e}_{E,i} \tag{A12}$$

$$\begin{aligned} &\vec{\omega}_{j_1} \bullet \left(-\vec{e}_{N,k} \times \vec{p}_k\right) + \vec{\omega}_{j_2} \bullet \left(\vec{e}_{N,k} \times \vec{p}_k\right) \\ &\quad = \left(a_k \delta\vec{G}_{SS,k} + b_k \vec{G}_{N,k}\right) \bullet \vec{e}_{N,k} \end{aligned} \tag{A13}$$

$$\begin{aligned} &\vec{\omega}_{j_1} \bullet \left(-\vec{e}_{E,k} \times \vec{p}_k\right) + \vec{\omega}_{j_2} \bullet \left(\vec{e}_{E,k} \times \vec{p}_k\right) \\ &\quad = \left(a_k \delta\vec{G}_{SS,k} + b_k \vec{G}_{N,k}\right) \bullet \vec{e}_{E,k} \end{aligned} \tag{A14}$$

[55] We regularize the inversion by introducing a stochastic damping parameter for each block rotation and fault slip parameter. For the Walker Lane model discussed in

section 4.2, we assigned the a priori uncertainty in slip rates to be 1.0 mm/yr and the a priori uncertainty in rotation rate of $10^{-8}$/yr.

[56] **Acknowledgments.** We would like to thank those energetic volunteers and professionals who assisted with the GPS data acquisition: Gerald Bawden, Rich Briggs, Jessica Murray, Fred Pollitz, Chuck Stiffler, Jim Sutton, Jerry Svarc, Mathilde Vergnolle, and Chuck Wicks. We also thank those at the USGS who shared campaign GPS data and those who make freely available the continuous GPS data from the BARD, BARGEN, and PANGA arrays. We also thank those at UNAVCO, Inc., and SOPAC for archiving and distributing these data. Comments from Rick Bennett and Tim Dixon improved this manuscript. This work was partially supported by a grant from NASA Solid Earth and Natural Hazards Program.

## References

Agnew, D. C. (1992), The time-domain behavior of power law noises, *Geophys. Res. Lett.*, *19*, 333–336.

Atwater, T., and J. Stock (1998), Pacific-North America plate tectonics of the Neogene southwestern United States; an update, *Int. Geol. Rev.*, *40*(5), 375–402.

Bell, J. W., C. M. dePolo, A. M. Sarna-Wojcicki, A. R. Ramelli, and C. E. Meyer (1999), Surface faulting and paleoseismic history of the 1932 Cedar Mountain earthquake area, west-central Nevada, and implications for modern tectonics of the Walker Lane, *Geol. Soc. Am. Bull.*, *111*(6), 791–807.

Bell, J. W., S. J. Caskey, A. R. Ramelli, and L. Guerrieri (2004), Pattern and rates of faulting in the central Nevada seismic belt, and paleoseismic evidence for prior belt-like behavior, *Bull. Seismol. Soc. Am.*, *94*(4), 1229–1254.

Bennett, R. A., W. Rodi, and R. E. Reilinger (1996), Global Positioning System constraints on fault slip rates in southern California and northern Baja, Mexico, *J. Geophys. Res.*, *101*, 21,943–21,960.

Bennett, R. A., B. P. Wernicke, and J. L. Davis (1998), Continuous GPS measurements of contemporary deformation across the northern Basin and Range province, *Geophys. Res. Lett.*, *25*, 563–566.

Bennett, R. A., B. P. Wernicke, N. A. Niemi, A. M. Friedrich, and J. L. Davis (2003), Contemporary strain rates in the northern Basin and Range province from GPS data, *Tectonics*, *22*(2), 1008, doi:10.1029/2001TC001355.

Bills, B. G., D. R. Currey, and G. A. Marshall (1994), Viscosity estimates for the crust and upper-mantle from patterns of shoreline deformation in the eastern Great Basin, *J. Geophys. Res.*, *99*, 22,059–22,086.

Bills, B. G., K. D. Adams, and S. G. Wesnousky (2007), Viscosity structure of the crust and upper mantle in western Nevada from isostatic rebound patterns of Lake Lahontan shorelines, *J. Geophys. Res.*, doi:10.1029/2005JB003941, in press.

Blewitt, G. (1989), Carrier phase ambiguity resolution for the Global Positioning System applied to geodetic baselines up to 2000 km, *J. Geophys. Res.*, *94*, 10,187–10,283.

Blewitt, G., and D. Lavallée (2002), Effect of annual signals on geodetic velocity, *J. Geophys. Res.*, *107*(B7), 2145, doi:10.1029/2001JB000570.

Blewitt, G., et al. (2005), A stable North America reference frame (SNARF): First release, paper presented at UNAVCO-IRIS Joint Workshop, Stevenson, Wash., 8–11 Jun.

Briggs, R. W., and S. G. Wesnousky (2005), Late Pleistocene and Holocene paleoearthquake activity of the Olinghouse fault zone, Nevada, *Bull. Seismol. Soc. Am.*, *95*, 1301–1313.

Caskey, J. S., J. W. Bell, B. D. Slemmons, and A. R. Ramelli (2000), Historical surface faulting and paleoseismology of the central Nevada seismic belt, in *Field Guide 2*, edited by D. R. Lageson, S. G. Peters, and M. M. Lahren, pp. 23–44, Geol. Soc. of Am., Boulder, Colo.

Clark, M. M., R. V. Sharp, R. O. Castle, and P. W. Harsh (1976), Surface faulting near Lake Oroville California in August, 1975, *Bull. Seismol. Soc. Am.*, *66*(4), 1101–1110.

d'Alessio, M. A., I. A. Johanson, R. Bürgmann, D. A. Schmidt, and M. H. Murray (2005), Slicing up the San Francisco Bay Area: Block kinematics and fault slip rates from GPS-derived surface velocities, *J. Geophys. Res.*, *110*, B06403, doi:10.1029/2004JB003496.

Davis, J. L., R. A. Bennett, and B. P. Wernicke (2003), Assessment of GPS velocity accuracy for the Basin and Range Geodetic Network (BARGEN), *Geophys. Res. Lett.*, *30*(7), 1411, doi:10.1029/2003GL016961.

Dixon, T. H., M. Miller, F. Farina, H. Wang, and D. Johnson (2000), Present-day motion of the Sierra Nevada block and some tectonic implications for the Basin and Range province, North American Cordillera, *Tectonics*, *19*, 1–24.

Dong, D., T. A. Herring, and R. W. King (1998), Estimating regional deformation from a combination of space and terrestrial geodetic data, *J. Geod.*, *72*, 200–214.

Dzurisin, D., M. P. Poland, and R. Bürgmann (2002), Steady subsidence of Medicine Lake volcano, northern California, revealed by repeated leveling surveys, *J. Geophys. Res.*, *107*(B12), 2372, doi:10.1029/2001JB000893.

Faulds, J. E., C. D. Henry, and N. H. Hinz (2005a), Kinematics of the northern Walker Lane: An incipient transform fault along the Pacific-North American plate boundary, *Geology*, *33*, 505–508, doi:10.1130/G21274.1.

Faulds, J. E., C. D. Henry, N. H. Hinz, P. S. Drakos, and B. Delwiche (2005b), Transect across the northern Walker Lane, northwest Nevada and northeast California: An incipient transform fault along the Pacific-North American plate boundary, in *Interior Western United States: Field Guide 6*, edited by J. Pederson and C. M. Dehler, pp. 129–150, Geol. Soc. of Am., Boulder, Colo.

Freed, A. M., and R. Burgmann (2004), Evidence of power-law flow in the Mojave Desert mantle, *Nature*, *430*, 548–551.

Gourmelen, N., and F. Amelung (2005), Post-seismic deformation in the central Nevada seismic belt detected by InSAR: Implications for Basin and Range dynamics, *Science*, *310*, 1473–1476.

Gourmelen, N., and F. Amelung (2006), Towards a continental scale deformation map of the Basin and Range by InSAR, *Eos Trans. AGU*, *86*(52), Fall Meet. Suppl., Abstract G51C-0845.

Hammond, W. C., and W. Thatcher (2004), Contemporary tectonic deformation of the Basin and Range province, western United States: 10 years of observation with the Global Positioning System, *J. Geophys. Res.*, *109*, B08403, doi:10.1029/2003JB002746.

Hammond, W. C., and W. Thatcher (2005), Northwest Basin and Range tectonic deformation observed with the Global Positioning System, 1999–2003, *J. Geophys. Res.*, *110*, B10405, doi:10.1029/2005JB003678.

Hammond, W. C., C. Kreemer, and G. Blewitt (2007), Geodetic constraints on contemporary deformation in the northern Walker Lane: 3, Postseismic relaxation in the Central Nevada Seismic Belt, in *Late Cenozoic Structure and Evolution of the Great Basin–Sierra Nevada Transition*, edited by J. Oldow and P. Cashman, Geol. Soc. of Am., Boulder, Colo., in press.

Hemphill-Haley, M. A., G. A. Carver, and B. Burke (1999), Late Quaternary stratigraphy and Holocene faulting along the eastern margin of Steens Mountain, southeastern Oregon, in *Quaternary Geology of the Northern Quinn River and Alvord Valleys, Southeastern Oregon*, edited by C. Narwold, Pac. Cell, Friends of the Pleistocene, Pasadena, Calif.

Hemphill-Haley, M. A., W. D. Page, G. A. Carver, and R. M. Burke (2000), Paleoseismicity of the Alvord fault, Steens Mountain, southeastern Oregon, in *Quaternary Geochronology: Methods and Applications*, *Ref. Shelf*, vol. 4, edited by J. Stratton Noller, J. M. Sowers, and W. R. Lettis, pp. 537–540, AGU, Washington, D. C.

Henry, C. D., J. E. Faulds, L. H. Garside, and N. H. Hinz (2003), Tectonic implications of ash-flow tuffs and paleovalley in the western US, *Geol. Soc. Am. Abstr. Programs*, *35*(6), 346.

Henry, C. D., J. E. Faulds, and C. M. dePolo (2007), Geometry and timing of strike-slip and normal faults of the northern Walker Lane, northwestern Nevada and northeastern California: Strain partitioning, sequential extension and strike-slip deformation, or both?, in *Late Cenozoic Structure and Evolution of the Great Basin–Sierra Nevada Transition*, edited by J. Oldow and P. Cashman, Geol. Soc. of Am., Boulder, Colo., in press.

Hetland, E. A., and B. H. Hager (2003), Postseismic relaxation across the Central Nevada Seismic Belt, *J. Geophys. Res.*, *108*(B8), 2394, doi:10.1029/2002JB002257.

Hill, D. P., J. O. Langbein, and S. Prejean (2003), Relations between seismicity and deformation during unrest in Long Valley Caldera, California, form 1995 through 1999, *J. Volcanol. Geotherm. Res.*, *127*(3–4), 175–193.

Hodgkinson, K. M., et al. (1996), Geometry of the 1954 Fairview Peak–Dixie Valley earthquake sequence from a joint inversion of leveling and triangulation data, *J. Geophys. Res.*, *101*, 25,437–425,457.

Humphreys, E. D., and M. A. Hemphill-Haley (1996), Causes and characteristics of western U.S. deformation, *Geol. Soc. Am. Abstr. Programs*, *28*(7), 2161996.

Jones, C. H., J. R. Unruh, and L. J. Sonder(1996), The role of gravitational potential energy in active deformation in the southwestern United States, *Nature*, *381*, 37–41.

Kreemer, C., G. Blewitt, and W. C. Hammond (2007), Geodetic constraints on contemporary deformation in the northern Walker Lane: 2, Velocity and tensor strain rate analysis, in *Late Cenozoic Structure and Evolution of the Great Basin–Sierra Nevada Transition*, edited by J. Oldow and P. Cashman, Geol. Soc. of Am., Boulder, Colo., in press.

Lahr, K. M., J. C. Lahr, A. G. Lindh, C. G. Bufe, and F. W. Lester (1976), The August 1975 Oroville Earthquakes, *Bull. Seismol. Soc. Am.*, *66*(4), 1085–1099.

Langbein, J., and H. Johnson (1997), Correlated errors in geodetic time series; implications for time-dependent deformation, *J. Geophys. Res.*, *102*, 591–604.

Mao, A. C., G. A. Harrision, and T. H. Dixon (1999), Noise in GPS coordinate time series, *J. Geophys. Res.*, *104*, 2797–2816.

McCaffrey, R. (2002), Crustal block rotations and plate coupling, in *Plate Boundary Zones*, *Geodyn. Ser.*, vol. 30, edited by S. Stein and J. Freymueller, pp. 101–122, AGU, Washington, D. C.

McCaffrey, R. (2005), Block kinematics of the Pacific–North America plate boundary in the southwestern United States from inversion of GPS, seismological, and geologic data, *J. Geophys. Res.*, *110*, B07401, doi:10.1029/2004JB003307.

McClusky, S. C., S. C. Bjornstad, B. H. Hagar, R. W. King, B. J. Meade, M. M. Miller, F. C. Monastero, and B. J. Souter (2001), Present-day kinematics of the eastern California shear zone from a geodetically constrained block model, *Geophys. Res. Lett.*, *28*, 3369–3372.

Meade, B. J., and B. H. Hager (2005), Block models of crustal motion in southern California constrained by GPS measurements, *J. Geophys. Res.*, *110*, B03403, doi:10.1029/2004JB003209.

Miller, M. M., D. J. Johnson, and T. H. Dixon (2001), Refined kinematics of the eastern California shear zone from GPS observations, 1993–1998, *J. Geophys. Res.*, *106*, 2245–2263.

Morrison, P. W., B. W. Stump, and R. Uhrhammer (1976), The Oroville earthquake sequence of August 1975, *Bull. Seismol. Soc. Am.*, *66*(4), 1065–1084.

Murray, M. H., and P. Segall (2001), Modeling broad scale deformation in northern California and Nevada from plate motions and elastic strain accumulation, *Geophys. Res. Lett.*, *28*, 4315–4318.

Nakiboglu, S. M., and K. Lambeck (1983), A reevaluation of the isostatic rebound of Lake Bonneville, *J. Geophys. Res.*, *88*, 10,439–10,447.

Nishimura, T., and W. Thatcher (2003), Rheology of the lithosphere inferred from postseismic uplift following the 1959 Hebgen Lake earthquake, *J. Geophys. Res.*, *108*(B8), 2389, doi:10.1029/2002JB002191.

Okada, Y. (1985), Surface deformation due to shear and tensile faults in a half-space, *Bull. Seismol. Soc. Am.*, *75*(4), 1135–1154.

Okada, Y. (1992), Internal deformation due to shear and tensile faults in a half-space, *Bull. Seismol. Soc. Am.*, *82*(2), 1018–1040.

Oldow, J. S. (2003), Active transtensional boundary zone between the western Great Basin and Sierra Nevada block, western U.S. Cordillera, *Geology*, *31*, 1033–1036.

Oldow, J. S., C. L. V. Aiken, J. L. Hare, J. F. Ferguson, and R. F. Hardyman (2001), Active displacement transfer and differential block motion within the central Walker Lane, western Great Basin, *Geology*, *29*, 19–22.

Pezzopane, S. K., and R. J. I. Weldon (1993), Tectonic role of active faulting in central Oregon, *Tectonics*, *12*, 1140–1169.

Pollitz, F. F., G. Peltzer, and R. Burgmann (2000), Mobility of continental mantle: Evidence from postseismic geodetic observation following the 1992 Landers earthquake, *J. Geophys. Res.*, *105*, 8035–8054.

Pollitz, F. F., C. W. Wicks, and W. Thatcher (2001), Mantle flow beneath a continental strike slip fault: Postseismic deformation after the 1999 Hector Mine earthquake, *Science*, *293*, 1814–1818.

Prawirodirdjo, L., et al. (1997), Geodetic observations of interseismic strain segmentation at the Sumatra subduction zone, *Geophys. Res. Lett.*, *24*, 2601–2604.

Savage, J. C. (1983), A dislocation model of strain accumulation and release at a subduction zone, *J. Geophys. Res.*, *88*, 4984–4996.

Savage, J. C., and R. O. Burford (1973), Geodetic determination of relative plate motion in central California, *J. Geophys. Res.*, *78*, 832–845.

Savage, J. C., and J. P. Church (1974), Evidence for postearthquake slip in the Fairview Peak, Dixie Valley, and Rainbow Mountain fault areas of Nevada, *Bull. Seismol. Soc. Am.*, *64*(3), 687–698.

Savage, J. C., M. Lisowski, W. H. Prescott, and J. P. Church (1977), Geodetic measurements of deformation associated with the Oroville, California, earthquake, *J. Geophys. Res.*, *82*, 1667–1671.

Savage, J. C., M. Lisowski, J. L. Svarc, and W. K. Gross (1995), Strain accumulation across the central Nevada seismic zone, 1973–1994, *J. Geophys. Res.*, *100*, 20,257–20,269.

Savage, J. C., W. Gan, and J. L. Svarc (2001), Strain accumulation and rotation in the eastern California shear zone, *J. Geophys. Res.*, *106*, 21,995–22,007.

Sawyer, T. L., R. W. Briggs, and A. R. Ramelli (2005), Late Quaternary activity of the southern Mohawk Valley fault zone, northeastern California, *Seismol. Res. Lett.*, *76*(2), 248.

Slemmons, B. D. (1957), Geological effects of the Dixie Valley–Fairview Peak, Nevada earthquakes of December 16, 1954, *Bull. Seismol. Soc. Am.*, *47*(4), 353–375.

Smith, K. D., D. von Seggern, G. Blewitt, L. Preston, J. G. Anderson, B. P. Wernicke, and J. L. Davis (2004), Evidence for Deep Magma injection beneath Lake Tahoe, Nevada-California, *Science*, *305*, 1277–1280.

Sonder, L. J., and C. H. Jones (1999), Western United States extension: How the West was widened, *Annu. Rev. Earth Planet. Sci.*, *27*, 417–462.

Souter, B. J. (1998), Comparisons of geological models to GPS observations in southern California, Ph.D. thesis, Mass. Inst. of Technol., Cambridge.

Svarc, J. L., J. C. Savage, W. H. Prescott, and A. R. Ramelli (2002), Strain accumulation and rotation in western Nevada, 1993–2000, *J. Geophys. Res.*, *107*(B5), 2090, doi:10.1029/2001JB000579.

Thatcher, W., and D. P. Hill (1991), Fault orientations in extensional and conjugate strike-slip environments and their implications, *Geology*, *19*, 1116–1120.

Thatcher, W., G. R. Foulger, B. R. Julian, J. L. Svarc, E. Quilty, and G. W. Bawden (1999), Present-day deformation across the Basin and Range province, western United States, *Science*, *283*, 1714–1718.

Unruh, J. R., J. Humphrey, and A. Barron (2003), Transtensional model for the Sierra Nevada frontal fault system, eastern California, *Geology*, *31*, 327–330.

Wdowinski, S., Y. Bock, J. Zhang, P. Fang, and J. Genrich (1997), Southern California permanent GPS geodetic array: Spatial filtering of daily positions for estimating coseismic and postseismic displacements induced by the 1992 Landers earthquake, *J. Geophys. Res.*, *102*, 18,057–18,070.

Wells, R. E., and R. W. Simpson (2001), Northward migration of the Cascadia forearc in the northwest U. S. and implications for subduction deformation, *Earth Planets Space*, *53*, 275–283.

Wernicke, B. P., and K. J. Snow (1998), Cenozoic tectonism in the central Basin and Range: Motion of the Sierran-Great Valley block, *Int. Geol. Rev.*, *40*, 403–410.

Wernicke, B. P., A. M. Friedrich, N. A. Niemi, R. A. Bennett, and J. L. Davis (2000), Dynamics of plate boundary fault systems from Basin and Range Geodetic Network (BARGEN) and geologic data, *GSA Today*, *10*(11), 1–7.

Wesnousky, S. G. (2005), Active faulting in the Walker Lane, *Tectonics*, *24*, TC3009, doi:10.1029/2004TC001645.

Wesnousky, S. G., A. D. Barron, R. W. Briggs, S. J. Caskey, S. Kumar, and L. Owen (2005), Paleoseismic transect across the northern Great Basin, *J. Geophys. Res.*, *110*, B05408, doi:10.1029/2004JB003283.

Williams, S. D. P. (2003a), Offsets in Global Positioning System time series, *J. Geophys. Res.*, *108*(B6), 2310, doi:10.1029/2002JB002156.

Williams, S. P. D. (2003b), The effect of coloured noise on the uncertainties of rates estimated from geodetic time series, *J. Geod.*, *76*, 483–494.

Williams, S. D. P., Y. Bock, P. Fang, P. Jamason, R. M. Nikolaidis, L. Prawirodirdjo, M. Miller, and D. J. Johnson (2004), Error analysis of continuous GPS position time series, *J. Geophys. Res.*, *109*, B03412, doi:10.1029/2003JB002741.

Wills, C. J., and G. Borchardt (1993), Holocene slip rate and earthquake recurrence on the Honey Lake fault zone, northeastern California, *Geology*, *21*, 853–856.

Zumberge, J. F., M. B. Heflin, D. C. Jefferson, M. M. Watkins, and F. H. Webb (1997), Precise point positioning for the efficient and robust analysis of GPS data from large networks, *J. Geophys. Res.*, *102*, 5005–5017.

W. C. Hammond, Nevada Bureau of Mines and Geology, University of Nevada, Reno, NV 89557, USA. (whammond@unr.edu)

W. Thatcher, Earthquake Hazards Team, U.S. Geological Survey, 345 Middlefield Road, MS 977, Menlo Park, CA 94025, USA.